Alma Mater Studiorum · University of Bologna

School of Science
Department of Physics and Astronomy
Master Degree in Physics

Detector induced charge asymmetry studies for future CP violation measurements at LHCb

Supervisor:
Prof. Angelo Carbone

Co-supervisor:
Dr. Laurent Dufour
Dr. Sascha Stahl

Submitted by:
Francesco Zenesini

Academic Year 2022/2023

Contents

Abstract

In this thesis it has been carried out a measurement of detection asymmetries A_{det} for the particle pair $K^-\pi^+$. The data analysed are Run 3 data that were collected by LHCb at centre-of-mass energy $\sqrt{s} = 13.6$ TeV during 2022 data taking campaign.

The decay mode studied are $D^+ \to K^-\pi^+\pi^+$ and $D^+ \to K^0_s\pi^+$. The dataset has been divided depending on the different requests of trigger: when the decays are triggered on signal tracks (TOS) or independently from the signal (TIS). The measurements have been carried independently in the two samples.

During these studies it was possible to study misalignment effects in early Run 3 data. The resulting integral detection asymmetries for both samples are

$$A^{\text{det}}_{\text{TIS}} = (-1.9 \pm 1.9)\%,$$
$$A^{\text{det}}_{\text{TOS}} = (-2.1 \pm 2.8)\%.$$

A differential measurement in bins of $p(K^-)$ for both samples have also been performed. The detection asymmetries are found to be compatible with zero.

With additional statistics from the full Run 3 data taking the measurement will become more precise and will be useful for future studies of production asymmetry measurements and CP violation measurements.

Sommario

In questa tesi è presentata la misura della asimmetria di rivelazione A_{det} per la coppia di particelle $K^-\pi^+$. I dati analizzati sono i dati del Run 3 che sono stati raccolti da LHCb ad una energia del centro di massa $\sqrt{s} = 13.6$ TeV nel 2022. I decadimeti studiati sono $D^+ \to K^-\pi^+\pi^+$ e $D^+ \to K^0_s\pi^+$. I dati sono stati divisi in due campioni a seconda del trigger utilizzat: quando le tracce del segnale hanno soddisfatto la condizione di trigger (TOS) o quando il trigger ha selezionato il segnale indipendentemente dalle tracce di segnale (TIS). Le misure sono state svolte in maniera indipendente nei due campioni.

Durante questi studi è stato possibile studiare effetti di disallineamento nei primi dati del Run 3. I risultati per le asimmetrie di rivelamento integrali per entrambi i campioni sono

$$A^{\text{det}}_{\text{TIS}} = (-1.9 \pm 1.9)\%,$$
$$A^{\text{det}}_{\text{TOS}} = (-2.1 \pm 2.8)\%.$$

Inoltre è stata svolta una misura differenziale in bin di $p(K^-)$ per entrambi i campioni. Le misure sono risultate compatibili con zero.

Includendo ulteriore statistica proveninete dall'intera campagna di presa dati del Run 3 la misura diventerà sempre più precisa e fondamentale per futuri studi di misure di asimmetrie di produzione e violazione di CP.

Introduction

One of the most powerful probes of physics beyond the Standard Model is the study of the combined charge conjugation and parity symmetry violation, the CP violation. Even if CP violation is predicted by the Standard Model, the entity of the predicted value is not enough to describe the asymmetry between matter and antimatter observed in the Universe. So, it is fundamental to search for new sources of CP violation.

The LHCb experiment is the world leading experiment in the field of flavour physics of both charm and beauty hadrons CP violation. With the increasing experimental success of the LHCb experiment it is become possible to reach higher and higher precision in measurement of CP asymmetry in the charm sector. Traditionally it was possible to cancel nuisance asymmetries with control decay channels. However, to investigate with more precision or to open the possibility to this kind of measurement in channels in which this method can not be applied, a precise knowledge of these asymmetries is required. In particular, production asymmetries are background effects in many CP violation searches, and they are of high interest thanks to the many other applications they have. Other than precision CP violation measurement they can also be used to probe non-perturbative QCD models, and they can be an important test for the newly upgraded LHCb detector.

One of the main source of background for both CP asymmetries and production asymmetries are detection asymmetries, i.e. asymmetries due to different reconstruction efficiency between charged particle and anti-particle. The main goal of this thesis is to measure the detection asymmetry A_{det} of the pair of particles $K^-\pi^+$ in view of future studies of production asymmetries and CP asymmetries, using Run 3 data collected by LHCb in 2022 at $\sqrt{s} = 13.6$ TeV. In particular, the $D^+ \to K^-\pi^+\pi^+$ and $D^+ \to K^0_s\pi^+$ decays have been analysed.

The thesis is structured as follows: in Chap. 1 the main theoretical aspects concerning CP violation and production asymmetries are reported; Chap. 2 focuses on the recently upgraded LHCb experimental apparatus, in particular on the main sub-detector relevant to this thesis work and Chap. 3 reports the analysis strategy in view of future measurements of production and CP violation asymmetries, the experimental method to extract the detection asymmetry of the pair $K^-\pi^+$ and the results.

Chapter 1

Theoretical Framework

This Chapter presents the main theoretical aspects for CP violation and production asymmetries. In Sec. 1.1, some topics of the Standard model, the electroweak theory, and the role of the CKM matrix are presented. Sec. 1.2 introduces the formalism for describing the different possible CP violation mode in meson systems and the main results in the charm meson sector in CP violation searches. Lastly, in Sec. 1.3 are described how production asymmetries can arise and some possible model that can explain the process.

1.1 The Standard Model

The Standard Model is a Yang-Mills theory, i.e. a non-Abelian quantum field theory based on the gauge symmetry groups $SU(3)_C \otimes SU(2)_L \otimes U(1)_Y$ with $SU(3)_C$ and $SU(2)_L$ non-Abelian groups responsible for, respectively, quantum chromodynamics and weak interactions and $U(1)_Y$ the Abelian group responsible for hypercharge interaction. $SU(2)_L \otimes U(1)_Y$ is the gauge symmetry group of electroweak theory referred as Glashow-Salam-Weinberg (GSM) model [1].

In the Standard Model fermions are organized in doublets of left-handed particle and right-handed singlet as [2]

$$\begin{aligned} q_L^i &= \begin{pmatrix} u \\ d \end{pmatrix}_L, \begin{pmatrix} c \\ s \end{pmatrix}_L, \begin{pmatrix} t \\ s \end{pmatrix}_L, & L_e^i &= \begin{pmatrix} \nu_e \\ e \end{pmatrix}_L, \begin{pmatrix} \nu_\mu \\ \mu \end{pmatrix}_L, \begin{pmatrix} \nu_\tau \\ \tau \end{pmatrix}_L, \\ u_R^i &= u_R, c_R, t_R, & e_R^i &= e_R, \mu_R, \tau_R, \\ d_R^i &= d_R, s_R, b_R, \end{aligned} \tag{1.1}$$

in which q_L^i are the left-handed quark doublet, L_e^i are the left-handed lepton doublet, u_R^i, d_R^i, e_R^i are right-handed up-like quarks, down-like quarks and charged leptons.

Each quark weak-isospin doublet have hypercharge $Y(q_L^i) = 1/3$ while leptons have $Y(L_e^i) = -1$. Right-handed up-like quarks have hypercharge $Y(u_R^i) = 4/3$, down-like quarks have hypercharge $Y(d_R^i) = -2/3$, while leptons have hypercharge $Y(e_R^i) = -2$ [2].

The gauge boson of the group $SU(2)_L \otimes U(1)_Y$ are

$$b^1_\mu, b^2_\mu, b^3_\mu \quad for\ SU(2)_L, \tag{1.2}$$

$$a_\mu \quad for\ U(1)_Y. \tag{1.3}$$

To ensure the proper symmetry breaking of Brout-Engler-Higgs (BEH) mechanism we also need to introduce a complex doublet of scalar fields Φ defined as

$$\Phi \equiv \begin{pmatrix} \Phi^+ \\ \Phi^0 \end{pmatrix}, \tag{1.4}$$

that is a $SU(2)_L$ doublet with hypercharge $Y(\Phi) = +1$.

The Lagrangian for electroweak theory can be written as [1–5]

$$\mathcal{L}_{EW} = \mathcal{L}_{gauge} + \mathcal{L}_{fermions} + \mathcal{L}_{scalar} + \mathcal{L}_{Yukawa}, \tag{1.5}$$

where $\mathcal{L}_{gauge}$ describes the four gauge bosons, $\mathcal{L}_{fermions}$ describes both quarks and leptons and their interaction with the gauge bosons, $\mathcal{L}_{scalar}$ describes the scalar complex doublet, its interaction with the gauge boson and how gauge boson acquire mass and $\mathcal{L}_{Yukawa}$ describes the interaction between fermions and the scalar and how fermions acquire mass after the spontaneous symmetry breaking (SSB).

The Lagrangian for the gauge bosons can be written as

$$\mathcal{L}_{gauge} = -\frac{1}{4} F^{i\mu\nu} F^i_{\mu\nu} - \frac{1}{4} f^{\mu\nu} f_{\mu\nu}, \tag{1.6}$$

where $F^i_{\mu\nu}$ is the field-strength tensor for the i-th gauge boson of $SU(2)_L$ and $f_{\mu\nu}$ is the field-strength tensor for $U(1)_Y$. $F^i_{\mu\nu}$ is defined as

$$F^i_{\mu\nu} = \partial_\nu b^i_\mu - \partial_\mu b^i_\nu + g\varepsilon_{ijk} b^j_\mu b^k_\nu, \tag{1.7}$$

with ε_{ijk} the structure constant of $SU(2)$, i.e. the Levi-Civita symbol and g the coupling of $SU(2)$. $f_{\mu\nu}$ is defined as

$$f_{\mu\nu} = \partial_\nu a_\mu - \partial_\mu a_\nu. \tag{1.8}$$

The fermion Lagrangian can be written as

$$\mathcal{L}_{fermions} = \overline{e_R}^i i\gamma^\mu D_\mu e^i_R + \overline{L_e}^i i\gamma^\mu D_\mu L^i_e + \overline{u_R}^i i\gamma^\mu D_\mu u^i_R + \overline{d_R}^i i\gamma^\mu D_\mu d^i_R + \overline{q_L}^i i\gamma^\mu D_\mu q^i_L, \tag{1.9}$$

where the covariant derivative D_μ is defined for singlets as

$$D_\mu = \partial_\mu + i\frac{g'}{2} a_\mu Y, \tag{1.10}$$

with g' the coupling constant of $U(1)_Y$. For doublets the covariant derivative is defined as

$$D_\mu = \partial_\mu + i\frac{g'}{2}a_\mu Y + i\frac{g}{2}\tau^i b^i_\mu, \tag{1.11}$$

where τ^i the generators of $SU(2)$. From the covariant derivative it is possible to derive the interaction terms between fermions and gauge bosons of electroweak theory.

The scalar Lagrangian can be written as

$$\mathcal{L}_{scalar} = (D^\mu\Phi)^\dagger(D_\mu\Phi) - V(\Phi^\dagger\Phi), \tag{1.12}$$

with the usual covariant derivative for the doublet and the potential that can be expressed as

$$V(\Phi^\dagger\Phi) = \mu^2(\Phi^\dagger\Phi) + |\lambda|(\Phi^\dagger\Phi)^2. \tag{1.13}$$

This term of the Lagrangian will allow the SSB of the BEH mechanism, and after that the covariant derivative applied to the scalar doublet will allow gauge bosons to have mass.

The Yukawa term of the Lagrangian is defined as

$$\mathcal{L}_{Yukawa} = -\zeta^i_e\overline{e^i_R}(\Phi^\dagger L^i) - \zeta^d_{ij}\overline{q_L}^i\Phi d^j_R - \zeta^u_{ij}\overline{q_L}^i\tilde{\Phi}u^j_R + h.c. \tag{1.14}$$

with $\tilde{\Phi} = i\sigma_2\Phi^*$ with σ_2 the second Pauli Matrix, ζ^i_e the three Yukawa coupling constants for leptons and $\zeta^d_{ij}, \zeta^u_{ij}$ are the 3×3 Yukawa matrices of couplings for, respectively, down-like quarks and up-like quarks.

After SSB and passage in unitary gauge, also known as U-gauge, Eq. 1.12 becomes

$$\begin{aligned}\mathcal{L}_{scalar} =& \frac{v^2}{8}\left[g^2|b^1_\mu - ib^2_\mu|^2 + (g'a_\mu - gb^3_\mu)^2\right] \\ &+ \frac{1}{2}\left[(\partial^\mu h)(\partial_\mu h) + 2\mu^2h^2\right] + \textit{interaction terms},\end{aligned} \tag{1.15}$$

with $v = 246.22$ GeV [2] the vacuum expectation value (VEV) of electroweak theory, and we can define the charged gauge bosons

$$W^\pm_\mu \equiv \frac{b^1_\mu \mp ib^2_\mu}{\sqrt{2}}, \tag{1.16}$$

and the orthogonal combinations

$$Z_\mu \equiv \frac{-g'a_\mu + gb^3_\mu}{\sqrt{g^2+g'^2}}, \tag{1.17}$$

$$A_\mu \equiv \frac{ga_\mu + g'b^3_\mu}{\sqrt{g^2+g'^2}}, \tag{1.18}$$

for the neutral gauge bosons of $SU(2)$ and the electromagnetic gauge boson, the photon. The Lagrangian has now a massive scalar boson h that is identified with the Higgs boson with mass $m_h = -2\mu^2$, three massive gauge bosons of $SU(2)$ with masses $m_W = gv/2$ and $m_Z = \sqrt{g^2 + g'^2}v/2$, and a massless gauge boson for electromagnetism.

With these redefinitions of the gauge bosons we can redefine the interaction Lagrangian between fermions and gauge bosons, i.e. from the covariant derivative of Eq. 1.9 as

$$\begin{aligned}\mathcal{L}_{fermions} =& g\left(W^+_\mu j^{\mu+}_W + W^-_\mu j^{\mu-}_W + Z^0_\mu j^m u_Z\right) + eA_\mu j^\mu_{EM} \\ &+ \textit{kinetic terms},\end{aligned} \tag{1.19}$$

where we have identified $e = gg'/\sqrt{g^2 + g'^2}$ the electric charge of the electron, j^μ_i are the current for the different processes and the kinetic terms are of the form $\overline{\Phi}^i i\partial_\mu \gamma^\mu \Psi^i$ for each fermion. The currents can be expressed as

$$\begin{aligned}j^{\mu+}_W =& \frac{1}{2\sqrt{2}}\sum_i (\bar{\nu}^i\gamma^\mu(1-\gamma^5)e^i + \bar{u}^i\gamma^\mu(1-\gamma^5)d^i), \\ j^{\mu-}_W =& \frac{1}{2\sqrt{2}}\sum_i (\bar{e}^i\gamma^\mu(1-\gamma^5)\nu^i + \bar{d}^i\gamma^\mu(1-\gamma^5)u^i), \\ j^\mu_Z =& \frac{1}{4\cos\theta_w}\sum_i \left[\overline{\Psi}^i\gamma^\mu(V_f - A_f\gamma^5)\Psi^i\right], \\ j^\mu_{EM} =& \sum_i Q_i\overline{\Psi}^i\gamma^\mu\Psi^i,\end{aligned} \tag{1.20}$$

where ν^i, e^i, u^i, d^i are neutrinos, charged leptons, up-like quarks and down-like quarks, $\cos\theta_w$, called weak mixing angle, is defined as $\cos\theta_w = g/\sqrt{g^2 + g'^2}$, Ψ^i in j^μ_Z are generic fermions, A_f, V_f are parameters that depend on the fermion it is currently considered, Ψ^i in j^μ_{EM} are any charged fermions with charge Q_i.

On the other hand to give mass to the fermions, the Yukawa term becomes

$$\begin{aligned}\mathcal{L}_{Yukawa} =& -\frac{v}{\sqrt{2}}(\zeta^i_e\overline{e_L}^i e^i_R + \overline{d_L}^i\zeta^d_{ij}d^j_R + \overline{u_L}^i\zeta^u_{ij}u^j_R) + h.c. \\ &+ \textit{interaction terms},\end{aligned} \tag{1.21}$$

where interactions terms between the Higgs boson and other fermions has been left implicit. The charged leptons have acquired a mass $m_e = v\zeta^i_e/\sqrt{2}$ where ζ^i_e are the Yukawa couplings for each charged lepton. Quarks' terms are still non-diagonal, in the so-called flavour basis, while the charged currents are diagonal as can be seen in Eq. 1.20. To obtain a proper mass term also for quarks, the two Yukawa matrices need to be diagonalized. Since these are complex matrices they can be diagonalized with the

following unitary transformation

$$\begin{aligned} d_L^i \to & U_d^{ij} d_L^j, \quad u_L^i \to U_u^{ij} u_L^j, \\ d_R^i \to & K_d^{ij} d_R^j, \quad u_R^i \to K_u^{ij} u_R^j, \end{aligned} \tag{1.22}$$

where U_d, U_u, K_d, K_u are 3×3 unitary matrices. With this transformation we pass from the flavour basis to the mass basis. We can rewrite the Yukawa matrices as

$$\zeta^d = U_d M_d K_d^\dagger, \quad \zeta^u = U_u M_u K_u^\dagger, \tag{1.23}$$

with M_d, M_u are real diagonal matrices with the masses of the quarks on the diagonal. The mass terms of Eq. 1.21 then becomes

$$\mathcal{L}_{mass} = -m_j^d \overline{d_L}^j d_R^j - m_j^u \overline{u_L}^j u_R^j + h.c. \tag{1.24}$$

with m_j^d, m_j^u the diagonal elements of $vM_d/\sqrt{2}, vM_u/\sqrt{2}$.

The kinetic terms of Eq. 1.19 and the neutral currents j_Z^μ, j_{EM}^μ of Eq. 1.20 are invariant under these transformations as U_d, U_u, K_d, K_u are unitary matrices and these terms do not mix different flavour of quarks. This is not true for charged current $j_W^{\mu\pm}$ that do mix up-like and down-like quarks as can be seen in Eq. 1.20. After this change of basis the resulting currents are

$$\begin{aligned} j_W^{\mu+} = & \frac{1}{2\sqrt{2}} \sum_i (\bar{\nu}^i \gamma^\mu (1-\gamma^5) e^i + \bar{u}^i \gamma^\mu (1-\gamma^5) U_u^{\dagger ik} U_d^{kj} d^j), \\ j_W^{\mu-} = & \frac{1}{2\sqrt{2}} \sum_i (\bar{e}^i \gamma^\mu (1-\gamma^5) \nu^i + \bar{d}^i \gamma^\mu (1-\gamma^5) U_u^{\dagger ik} U_d^{kj} u^i), \end{aligned} \tag{1.25}$$

where the lepton part has been left unchanged. We can define the Cabibbo-Kobayashi-Maskawa (CKM) matrix as

$$V^{ij} \equiv U_u^{\dagger ik} U_d^{kj} = \begin{pmatrix} V_{11} & V_{12} & V_{13} \\ V_{21} & V_{22} & V_{23} \\ V_{31} & V_{32} & V_{33} \end{pmatrix} = \begin{pmatrix} V_{ud} & V_{us} & V_{ub} \\ V_{cd} & V_{cs} & V_{cb} \\ V_{td} & V_{ts} & V_{tb} \end{pmatrix}, \tag{1.26}$$

that is a complex unitary matrix.

1.1.1 CKM Matrix

The CKM matrix is a 3×3 complex unitary matrix that describe the mixing of the interactions of the quark flavours in the mass basis. This mixing arises from the diagonalization of the Yukawa matrices as described in the previous Section.

Since the CKM is a complex matrix it can have up to $2n^2$ real parameters, where n is the dimension of the matrix, but it is also a unitary matrix that implies the relations:

$$\sum_i V_{ij} V_{ik}^* = \delta_{jk}. \tag{1.27}$$

This provides n^2 constraint so that the CKM can have $n^2 = 9$ real parameters. Of these nine parameters three are angles and six are phases.

After the transformation of Eq. 1.22 the various quark fields have a residual $U(1)^6$ global symmetry, meaning they are invariant under the following transformations

$$d_L^j \to e^{i\alpha_j} d_L^j, \quad d_R^j \to e^{i\alpha_j} d_R^j, \quad u_L^j \to e^{i\beta_j} u_L^j, \quad u_R^j \to e^{i\beta_j} u_R^j, \tag{1.28}$$

where j is not summed, with six angles α_j, β_j.

While the mass term of Eq. 1.24 is invariant under these transformations for any angle α_j, β_j the CKM matrix is invariant only if $\alpha_j = \beta_j = \theta$ that will bring 5 additional constraint on the phases.

The CKM matrix has then four degrees of freedom: three real angles $\theta_{12}, \theta_{23}, \theta_{13}$ and a phase δ. This allows us to parametrize the CKM matrix as

$$V = \begin{pmatrix} c_{12}c_{13} & s_{12}c_{13} & s_{13}e^{-i\delta} \\ -s_{12}c_{23} - c_{12}s_{23}s_{13}e^{i\delta} & c_{12}c_{23} - s_{12}s_{23}s_{13}e^{i\delta} & s_{23}c_{13} \\ s_{12}s_{23} - c_{12}c_{23}s_{13}e^{i\delta} & -c_{12}s_{23} - s_{12}c_{23}s_{13}e^{i\delta} & c_{23}c_{13} \end{pmatrix}, \tag{1.29}$$

where $c_{ij} \equiv \cos\theta_{ij}$ and $s_{ij} \equiv \sin\theta_{ij}$ with i, j are family labels. These angles can be chosen to be in the first quadrant so that $s_{ij}, c_{ij} \geq 0$. The currently measured values of these parameters are

$$\begin{aligned} &\sin\theta_{12} = 0.22500 \pm 0.00067, \quad &&\sin\theta_{13} = 0.00369 \pm 0.00011, \\ &\sin\theta_{23} = 0.04182^{+0.00085}_{-0.00074}, &&\delta = 1.144 \pm 0.027. \end{aligned} \tag{1.30}$$

We can note that all rotational angles are relative small so that the CKM matrix is nearly diagonal, and to a good approximation θ_{23} and θ_{13} elements are negligible while θ_{12}, the Cabibbo angle, provides all the flavour mixing. By defining the four following parameters

$$\begin{aligned} &\lambda \equiv \sin\theta_{12}, &&A \equiv \frac{s_{23}}{s_{12}^2}, \\ &\rho \equiv \mathrm{Re}\left(\frac{s_{13}e^{-i\delta}}{s_{12}s_{23}}\right), \quad &&\eta \equiv -\,\mathrm{Im}\left(\frac{s_{13}e^{-i\delta}}{s_{12}s_{23}}\right), \end{aligned} \tag{1.31}$$

and we can rewrite the CKM matrix in the Wolfestain parametrization

$$V = \begin{pmatrix} 1 - \frac{1}{2}\lambda^2 & \lambda & A\lambda^3(\rho - i\eta) \\ -\lambda & 1 - \frac{1}{2}\lambda^2 & A\lambda^2 \\ A\lambda^3(1 - \rho - i\eta) & -A\lambda^2 & 1 \end{pmatrix} + \mathcal{O}(\lambda^4). \tag{1.32}$$

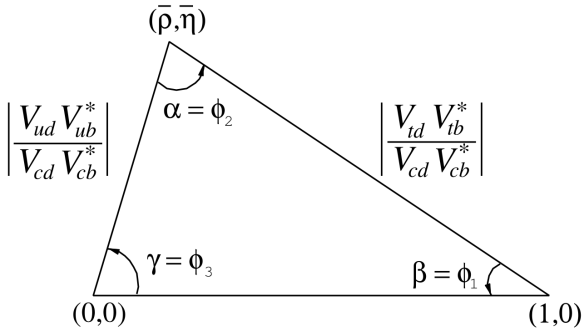

Figure 1.1: Unitarity triangle for $V_{ud}V_{ub}^* + V_{cd}V_{cb}^* + V_{td}V_{tb}^* = 0$.

The present measurements of each element of the CKM matrix are:

$$\begin{pmatrix} |V_{ud}| = 0.97373 \pm 0.00031 & |V_{us}| = 0.2243 \pm 0.0008 & |V_{ub}| = (3.82 \pm 0.20) \times 10^{-3} \\ |V_{cd}| = 0.221 \pm 0.004 & |V_{cs}| = 0.975 \pm 0.006 & |V_{cb}| = (40.8 \pm 1.4) \times 10^{-3} \\ |V_{td}| = (8.6 \pm 0.2) \times 10^{-3} & |V_{ts}| = (41.5 \pm 0.9) \times 10^{-3} & |V_{tb}| = 1.014 \pm 0.029 \end{pmatrix}. \tag{1.33}$$

Here is again clear how the matrix is nearly diagonal with elements ~ 1 on the diagonal. We can represent the unitarity propriety of the CMK matrix graphically with the unitarity triangle. From the unitarity relations of Eq. 1.27 we can write one of the relation

$$\frac{V_{ud}V_{ub}^*}{V_{cd}V_{cb}^*} + \frac{V_{td}V_{tb}^*}{V_{cd}V_{cb}^*} + 1 = 0, \tag{1.34}$$

that we can represent as a triangle in the complex plane as shown in Fig. 1.1. Six unitarity triangle exist, one for each condition in which $j \neq k$ of Eq. 1.27, but this is the most commonly used. From Eq. 1.31 we can also define the parameters $\bar{\rho} = \rho(1-\lambda^2/2+\mathcal{O}(\lambda^4))$ and $\bar{\eta} = \eta(1 - \lambda^2/2 + \mathcal{O}(4))$ so that the unitary triangle vertex is exactly $(\bar{\rho}, \bar{\eta})$. The three angles α, β, γ for this triangle can be defined as

$$\alpha = \arg\left(-\frac{V_{td}V_{tb}^*}{V_{ud}V_{ub}^*}\right), \quad \beta = \arg\left(-\frac{V_{cd}V_{cb}^*}{V_{td}V_{tb}^*}\right), \quad \gamma = \arg\left(-\frac{V_{ud}V_{ub}^*}{V_{cd}V_{cb}^*}\right). \tag{1.35}$$

The area of each unitary triangle is the same and is related to the Jarlskog invariant J as

$$J = 2(\text{area}) = \text{Im}(V_{ud}V_{tb}V_{td}^*V_{ub}^*). \tag{1.36}$$

and since it is related to the imaginary part of the CKM matrix, having a real CKM matrix would imply $J = 0$ and the unitary triangle would collapse into a line. The Jarlskog invariant is defined as:

$$J\sum_{m,n}\varepsilon_{ikm}\varepsilon_{jln} = \text{Im}(V_{ij}V_{kl}V_{il}^*V_{kj}^*), \tag{1.37}$$

and is closely related to CP violation in the quark sector of electroweak theory. In the parametrization of Eq. 1.29 it can be expressed also as:

$$J = s_{12}s_{23}s_{31}c_{12}c_{23}c_{31}^2 \sin\delta. \tag{1.38}$$

CP violation arises from the quark interaction term of Eq. 1.19. Under CP symmetry the term is invariant if $V = V^*$, so a non-zero phase implies CP violation if the Yukawa matrices are real and diagonal. This can be done simultaneously with a real CKM matrix only if

$$-iC = [Y_u, Y_d] = 0, \tag{1.39}$$

where we have defined the traceless Hermitian matrix C which determinant is proportional to the CP violation in the weak sector of the Standard Model. It can be expressed as

$$\det C = -\frac{16}{v^6}(m_t - m_c)(m_t - m_u)(m_b - m_s)(m_b - m_d)(m_s - m_d)J, \tag{1.40}$$

where v is the VEV of the electroweak theory. To have CP violation in the standard model the following conditions need to be respected

- up-like quarks and down-like quarks masses must not be degenerate;
- all mixing angle $\theta_{12}, \theta_{23}, \theta_{13}$ need to be different from zero and $\pi/2$ while the phase δ needs to be different from 0 and π;
- the phase of the CKM matrix needs to be different from zero.

Having three generation of quarks is required to have a complex CKM matrix, as with only two generation the CKM matrix is real.

1.2 CP Violation in mesons systems

This Section focuses on the phenomenology of mesons systems with a classification of CP violation effects for both charged and neutral mesons with a particular emphasis on charm mesons $D^{\pm}$ and D^0. The general formalism is the same for different flavour mesons with small difference depending on the particular flavour.

We can define the following amplitude for a particle P and its CP conjugate $\overline{P}$

$$\begin{aligned} A_f &= \langle f|H|P\rangle\,, \quad \overline{A}_f = \langle f|H|\overline{P}\rangle\,, \\ A_{\overline{f}} &= \langle \overline{f}|H|P\rangle\,, \quad \overline{A}_{\overline{f}} = \langle \overline{f}|H|\overline{P}\rangle\,, \end{aligned} \tag{1.41}$$

where f is a final state, $\overline{f}$ its CP conjugate and H is the Hamiltonian of the weak interactions.

As we have seen before, the CKM matrix introduces a phase in the interaction term that will appear in the final amplitude. This phase ϕ_i, called weak phase will be of opposite sign for A_f and $\overline{A}_{\bar{f}}$. However, also if the Lagrangian is real, an additional phase can arise from intermediate on-shell states. This is usually due to strong interaction and is referred to as strong phase δ_i and do not change sign under CP conjugation. The amplitudes of Eq. 1.41 can be rewritten as

$$A_f = \sum_i |A_i| e^{i(\delta_i + \phi_i)}, \quad \overline{A}_{\bar{f}} = \sum_i |A_i| e^{i(\delta_i - \phi_i)}, \tag{1.42}$$

where A_j are the amplitudes of each possible process.

For charged mesons the only possible physical CP violation observable is the asymmetry that we can define as

$$A_{CP} = \frac{\Gamma(P \to f) - \Gamma(\overline{P} \to \bar{f})}{\Gamma(P \to f) + \Gamma(\overline{P} \to \bar{f})} = \frac{|A_f|^2 - |\overline{A}_{\bar{f}}|^2}{|A_f|^2 + |\overline{A}_{\bar{f}}|^2}, \tag{1.43}$$

that is CP violating if $|\overline{A}_{\bar{f}}/A_f| \neq 1$ This is due to the difference of phase of the amplitudes from Eq. 1.42 as

$$|A_f|^2 - |\overline{A}_{\bar{f}}|^2 = -2 \sum_{i,j} |A_i||A_j| \sin(\delta_i - \delta_k) \sin(\phi_i - \phi_j), \tag{1.44}$$

so that to have an observable CP violation at least two process with different weak and strong phases are needed.

For neutral meson there can be additional CP violation source as the neutral mesons can oscillate or mix. We can define an initial state that is a superposition of the states $|P\rangle$ and $|\overline{P}\rangle$ as

$$|\Psi(0)\rangle = a(0)\,|P\rangle + b(0)\,|\overline{P}\rangle\,, \tag{1.45}$$

and its time evolving one

$$|\Psi(t)\rangle = a(t)\,|P\rangle + b(t)\,|\overline{P}\rangle\,. \tag{1.46}$$

Assuming the Weisskopf–Wigner approximation, in which time scales of the time evolution are much larger than strong time scales we can express the time evolution with the Schrödinger equation

$$i\hbar \frac{\partial}{\partial t} \Psi = \mathcal{H} \Psi, \tag{1.47}$$

where the Hamiltonian $\mathcal{H}$ can be expressed as

$$\mathcal{H} = \mathbf{M} - \frac{i}{2}\mathbf{\Gamma} = \begin{pmatrix} M_{11} - \frac{i}{2}\Gamma_{11} & M_{12} - \frac{i}{2}\Gamma_{12} \\ M_{21} - \frac{i}{2}\Gamma_{21} & M_{22} - \frac{i}{2}\Gamma_{22} \end{pmatrix}, \tag{1.48}$$

where $\mathbf{M}$ and $\mathbf{\Gamma}$ are 2×2 Hermitian matrices. The diagonal terms are associated with flavour conserving transition while off-diagonal terms are associated with flavour-changing transitions. From CPT invariance we can derive that $M_{11} = M_{22}$ and $\Gamma 11 = \Gamma_{22}$ and we can derive that $M_{12} = M_{21}^*$ and $\Gamma_{12} = \Gamma_{21}^*$.

The eigenstates of this Hamiltonian are:

$$\begin{aligned} |P_1\rangle =& p\,|P\rangle + q\,|\overline{P}\rangle\,, \\ |P_2\rangle =& p\,|P\rangle - q\,|\overline{P}\rangle\,, \end{aligned} \tag{1.49}$$

with eigenvalues:

$$\begin{aligned} M_1 - \frac{i}{2}\Gamma_1 =& M_{11} - \frac{i}{2}\Gamma_{11} + \frac{q}{p}(M_{12} - \frac{i}{2}\Gamma_{12}), \\ M_2 - \frac{i}{2}\Gamma_2 =& M_{11} - \frac{i}{2}\Gamma_{11} - \frac{q}{p}(M_{12} - \frac{i}{2}\Gamma_{12}), \end{aligned} \tag{1.50}$$

with q and p defined as:

$$\frac{q}{p} = \pm\sqrt{\frac{M_{12}^* - \frac{i}{2}\Gamma_{12}^*}{M_{12} \frac{i}{-} 2\Gamma_{12}}}, \tag{1.51}$$

where the choice of the minus sign would imply switching $1 \to 2$ states of Eq. 1.49. Considering time evolution and inverting the relation to obtain the time evolution of the single states $|P\rangle$ and $|\overline{P}\rangle$ we obtain:

$$\begin{aligned} |P\rangle =& g_+(t)\,|P\rangle - \frac{q}{p} g_-(t)\,|\overline{P}\rangle\,, \\ |\overline{P}\rangle =& g_+(t)\,|\overline{P}\rangle - \frac{q}{p} g_-(t)\,|P\rangle\,. \end{aligned} \tag{1.52}$$

with:

$$g_\pm(t) = \frac{1}{2}\left[\exp\left(-iM_1 t - \frac{1}{2}\Gamma_1 t\right) \pm \exp\left(-iM_2 - \frac{1}{2}\Gamma_2 t\right)\right]. \tag{1.53}$$

For neutral mesons there are three possible CP violation mechanism

- CP violation in the decay as for charged mesons if

$$|A_f/\overline{A}_f| \neq 1 \tag{1.54}$$

  called direct CP violation;

- CP violation in the mixing if

$$|q/p| \neq 1; \tag{1.55}$$

- CP violation in the interference between a decay with mixing and one without mixing with the same final state $f = \overline{f}$. This occurs if

$$\mathrm{Im}\left(\frac{q\overline{A}_f}{pA_f}\right) \neq 0, \tag{1.56}$$

  and can happen also if condition of the first two kind are not satisfied.

1.2.1 CP violation in Charm Mesons

CP violation in charm mesons has been observed for the first time in 2019 by the LHCb collaboration [6]. The most sensitive searches involve $D^0 \to K^+K^-$, $D^0 \to \pi^+\pi^-$ and $D^0 \to K^\pm\pi^\mp$. We can divide the time integrated CP violation asymmetry in three contribution similar to the three mode for CP violation as presented in the previous section. In the Standard Model the mixing and interference contributions are negligible with respect to the direct contribution. We can define

$$\Delta A_{CP} \equiv a^d_{K^+K^-} - a^d_{\pi^+\pi^-}, \tag{1.57}$$

where $a^d_{K^+K^-}, a^d_{\pi^+\pi^-}$ are the contribution of direct CP violation for respectively $D^0 \to K^+K^-$ and $D^0 \to \pi^+\pi^-$. The current average gives $\Delta A_{CP} = (-0.164 \pm 0.028) \times 10^{-2}$ [5, 7]. To measure CP violation due to mixing or to the interference between mixing and decay for charm mesons we need to analyse the time dependence of the decay rate that is modified by mixing so that the decay rate parameter becomes [5]

$$\begin{aligned} \Gamma_{D^0\to K^+K^-} =& \Gamma \times [1 + |q/p|(y\cos\Phi_D - x\sin\Phi_D)], \\ \Gamma_{\overline{D^0}\to K^+K^-} =& \Gamma \times [1 + |q/p|(y\cos\Phi_D - x\sin\Phi_D)], \end{aligned} \tag{1.58}$$

where Γ is the true decay width, $x = (M_1 - M_2)/\Gamma$ and $y = (\Gamma_1 - \Gamma_2)/2\Gamma$ the mixing parameters and Φ_D is defined as $\Phi_D = \arg(q\overline{A}_{\bar{f}}/pA_f)$. From these decay widths we can define

$$\begin{aligned} y_{CP} \equiv& \frac{\Gamma_{\overline{D^0}\to K^+K^-} + \Gamma_{D^0\to K^+K^-}}{2\Gamma} - 1, \\ A_\Gamma \equiv& \frac{\Gamma_{D^0\to K^+K^-} - \Gamma_{\overline{D^0}\to K^+K^-}}{2\Gamma}, \end{aligned} \tag{1.59}$$

which in presence of CP conservation should be $y_{CP} = y = (0.62 \pm 0.006) \times 10^{-2}$. The present measurements have obtained [7]

$$\begin{aligned} y_{CP} =& (+0.72 \pm 0.11) \times 10^{-2}, \\ A_\Gamma =& (0.009 \pm 0.011) \times 10^{-2}. \end{aligned} \tag{1.60}$$

There are also no indication for CP violation from the time-dependent analysis of $D^0 \to K_s\pi^+\pi^-$ from which is possible to extract $|q/p|$ and Φ_D that have been measured to be $1 - |q/p| = +0.005 \pm 0.016$ and $\Phi_D = (-2.5 \pm 1.2)^\circ$ [5] compatible with the CP conservation hypothesis.

Finally, also in charged D mesons there are searches for CP violation in Cabibbo suppressed decays. Currently, the most precise ones are from direct CP violation in $D^+ \to K_sK^+$ with a CP asymmetry of $A^{CP}_{D^+\to K_sK^+} = 0.0011 \pm 0.0017$ [5] and $D^+_s \to K_s\pi^+$ with $A^{CP}_{D^+_s\to K_s\pi^+} = +0.0038 \pm 0.0048$ [5].

1.3 Production Asymmetries and Hadronization Effects

In fixed-target experiment the production of D mesons has been observed to have a large asymmetry due to the leading particle effect [8]. This effect consist in a higher production of charmed mesons which share a valence parton with the hadron beam. In particular, the E791 experiment at Fermilab observed an abundance of $D^-(\bar{c}d)$ production over $D^+(c\bar{d})$ when these mesons are produced along the direction of the beam. The beam itself was composed of $\pi^-(\bar{u}d)$ at 500 GeV. The production asymmetry can be defined as

$$A_{\text{prod}}(D^+) = \frac{d\sigma(D^+) - d\sigma(D^-)}{d\sigma(D^+) + d\sigma(D^-)}, \tag{1.61}$$

where $\sigma(D^\pm)$ are production cross-section for $D^\pm$. In the E791 experiment the observed asymmetry was $A_{\text{prod}} \sim 0.7$. However, the QCD factorization theorem for heavy quark production states that the cross-section for a D meson can be written as

$$d\sigma(hh' \to D + X) = \sum_{i,j} f_{i/h} \otimes f_{j/h'} \otimes d\hat{\sigma}(ij \to c\bar{c} + X) \otimes D_{c\to D} + \mathcal{O}(\Lambda_{\text{QCD}}/m_c), \tag{1.62}$$

where $f_{i/h}$ and f_j/h' are the distributions functions for the partons, respectively i, j in the hadrons h, h', $d\hat{\sigma}(ij \to c\bar{c}+X)$ is the parton cross-section and $D_{c\to D}$ is the fragmentation function for the hadronization of a c quark into a D meson. At leading order the processes $gg \to c\bar{c}$ and $q\bar{q} \to c\bar{c}$ produces charm quarks symmetrically. Furthermore, charge conjugation invariance implies that $D_{c\to D} = D_{\bar{c}\to\overline{D}}$ so no production asymmetry is expected.

So these high asymmetries are produced at next-to-leading order. Thanks to this, measuring production asymmetries can probe different models for these power corrections and can help determine additional parameters of QCD. In particular, we will shortly present two different models: the intrinsic charm coalescence model [9] and the heavy-quark recombination mechanism [8].

Coalescence is the process by which a produced charm quark forms charmed hadrons by combining with similar rapidities quarks. In particular, it is possible that the heavy quarks will coalescence with the spectator valence quarks of the projectile. Higher coalescence probability will occur when the two quarks have low relative rapidity and low transverse momentum [9].

In heavy-quark-recombination the charm quark will recombine with a light parton that have taken part in the hard-scattering process rather than the spectators. In this model only a single more parameter is needed to properly explain observed production asymmetries.

Production asymmetry has already been measured for $D^\pm$ at LHCb during Run 1 data taking and for $D_s^\pm$. For $D^\pm$ the resulting production asymmetry has been measured

to be [10]:

$$A_{\rm prod}(D^+) = (-0.96 \pm 0.26(\text{stat}) \pm 0.18(\text{syst}))\%, \tag{1.63}$$

with no significant dependence on p_T and η, while for $D_s^\pm$ has been measured to be [11]

$$A_{\rm prod}(D_s^+) = (-0.52 \pm 0.13(\text{stat}) \pm 0.10(\text{syst}))\%, \tag{1.64}$$

with no significant kinematic dependence.

Chapter 2

The LHCb Experiment

The LHCb Experiment is one of the four main experiment at the Large Hadron Collider (LHC) [12] at CERN. Its original main purpose was to perform high precision measurement of CP violation with D and B mesons as well as search for rare decays [13]. However, during both Run 1 and Run 2 the experiment has been able to reach and overcome the design performance working at higher luminosity than expected. The experiment was able to perform measurements in wider physics scopes while also reaching unprecedented precisions in the Flavour Physics sector [14].

In particular, it was able to perform the first measurement of CP violation in the charm sector [6]. For these reasons, the Upgrade 1 of the experiment was designed with particular attention to a broader physics programme. In this way LHCb has now become a general purpose detector in the forward region.

Understanding properly the newly upgrade detector is one of the current main challenge the LHCb collaboration is facing, and it is of fundamental importance for the upcoming analysis that will be carried on with Run 3 data.

In this Chapter, it is discussed the upgraded detector and its main features focusing on the most relevant sub-detectors related to the thesis work.The trigger system and how the detector can introduce some asymmetries in the physics analysis is also described.

2.1 The LHC Accelerator and Detector Layout

LHC is the world-largest synchrotron installed in the 26.7 km underground tunnel that previously hosted the Large Electron Positron collider (LEP) [15]. It is a proton-proton collider that has reached a centre of mass energy of $\sqrt{s} = 13.6$ TeV with a luminosity of $\mathcal{L} = 2 \times 10^{33}$ cm^{-2}s^{-1} during Run 3 data-taking campaign.

LHC is composed of 1232 superconducting magnetic dipoles that provide a nominal magnetic field of 8.33 T cooled at 1.9 K by superfluid helium, to curve the trajectory of the beams, and 392 quadrupoles that, along with other multipoles magnets, help focus

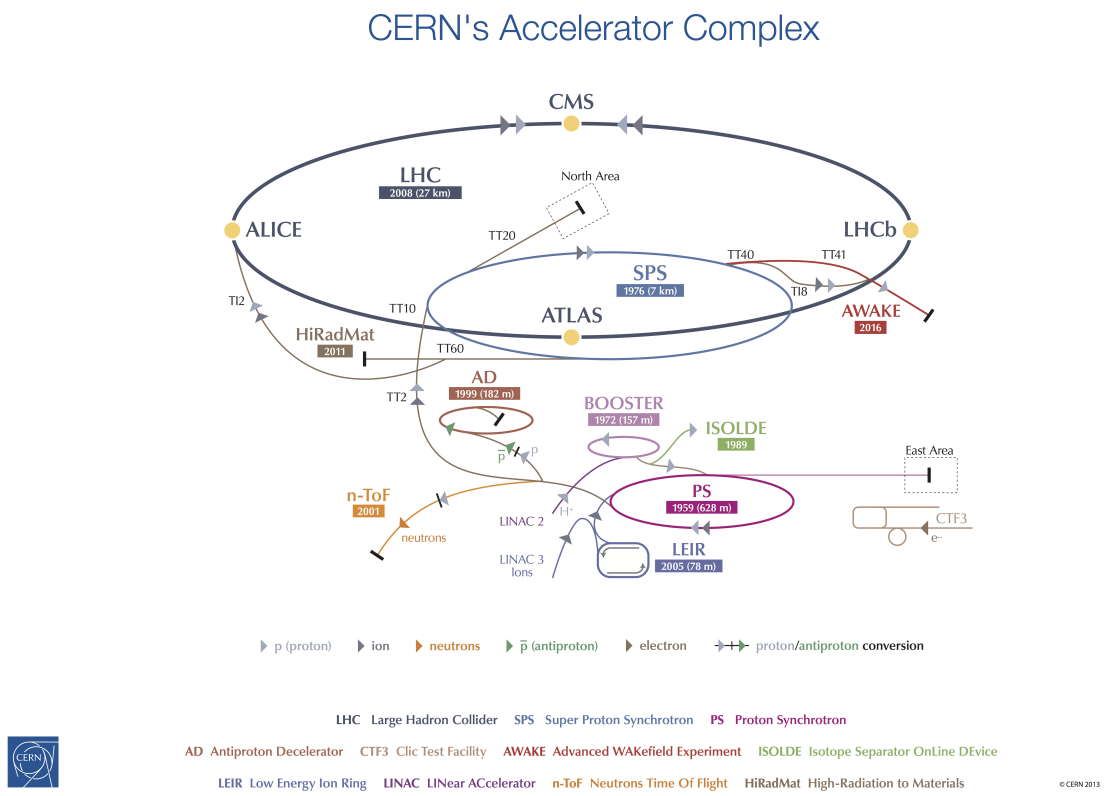

Figure 2.1: LHC accelerator complex [16]

and correct the trajectory of protons. Protons are accelerated with 400 MHz Radio Frequency (RF) system.

LHC is the last and most powerful accelerator of the complex of accelerators present at CERN as illustrated in Fig. 2.1. This complex, which one of the main goal is to inject protons in LHC, also serves many other experiments e.g. the Super Proton Synchrotron (SPS) between fills of LHC serves experiments located in the North Area.

LHC hosts four main experiments: ATLAS, CMS, LHCb and ALICE. LHCb is located at Interaction Point 8. It is a single-arm spectrometer in the forward region with a nominal pseudo-rapidity coverage of $2 < \eta < 5$. A schematic side view is present in Fig. 2.2. As showed in the schematic, the coordinate system is defined with the origin in the primary interaction point, the positive z-axis pointing towards the Muon System, the positive y-axis pointing vertically upwards and the x-axis is defined to obtain a right-handed system.

The experiment is equipped with a new tracking system with respect to the Run 1-2, composed of different sub-detector: the Vertex Locator (VELO), the Upstream Tracker

(UT), the Scintillating Fibres Tracker (SciFi).

The VELO is composed of pixelated hybrid silicon detectors near the interaction point. The UT is located before the magnet and is composed of silicon detectors. However, this sub-detector was not yet installed during 2022 data taking. The SciFi Tracker is the last element of the tracking system and is placed after the magnet. This sub-detector is composed of scintillating fibres paired with silicon photomultipliers (SiPM). A more in-depth discussion of the tracking system will be carried out in Sec. 2.2.

Two Ring Imagining Cherenkov (RICH1 and RICH2) detectors are used to identify particles alongside with an electromagnetic calorimeter (ECAL), a hadronic calorimeter (HCAL), and the muon system (M2-5).

The ECAL is a shashlik-type calorimeter composed of lead and scintillator with photomultiplier tubes (PMT) readout. The HCAL is a sampling calorimeter composed of iron and plastic scintillator with the same PMT type readout as the ECAL. Both ECAL and HCAL has not been modified from Run 1-2. RICH detectors, which were upgraded from Run 1-2, use as radiator, respectively, C_4F_{10} and CF_4. RICH1 is placed between the VELO and the UT and can identify lower momentum particles while RICH2 is placed between the SciFi Tracker and the ECAL and can identify higher momentum particles. The muon system is the last element of LHCb and is composed of four station that host 1104 MultiWire Proportional Chamber (MWPC) with iron absorber between each station. We will briefly discuss the particle identification system in Sec. 2.3.

The dipole magnet has not been modified from Run 1-2. It is a warm magnet able to provide a bending power of $\simeq 4$ T m for tracks generated near the primary interaction point [17]. During data taking its polarity is inverted every few weeks to have sample for both polarities of similar size.

2.2 Tracking System

The tracking system has been fully replaced from Run 1-2 while keeping its function to measure tracks' momentum. To do so two sub-detectors are placed before the magnet (VELO, UT) and one is placed after (SciFi). Measuring the bending of the track provoked by the magnet allows reconstructing the particle momentum.

In Run 3, reconstruction is performed in real-time at the trigger level to allow identifying the specific signal of interest.

The new tracking system of LHCb has more strict requirement to maintain the same or better physics performance of Run 1-2 while providing readout at a frequency of 40 MHz and accounting for the increased luminosity and pile-up of Run 3.

During 2022 data taking the UT sub-detector was still not installed and will not be further discussed.

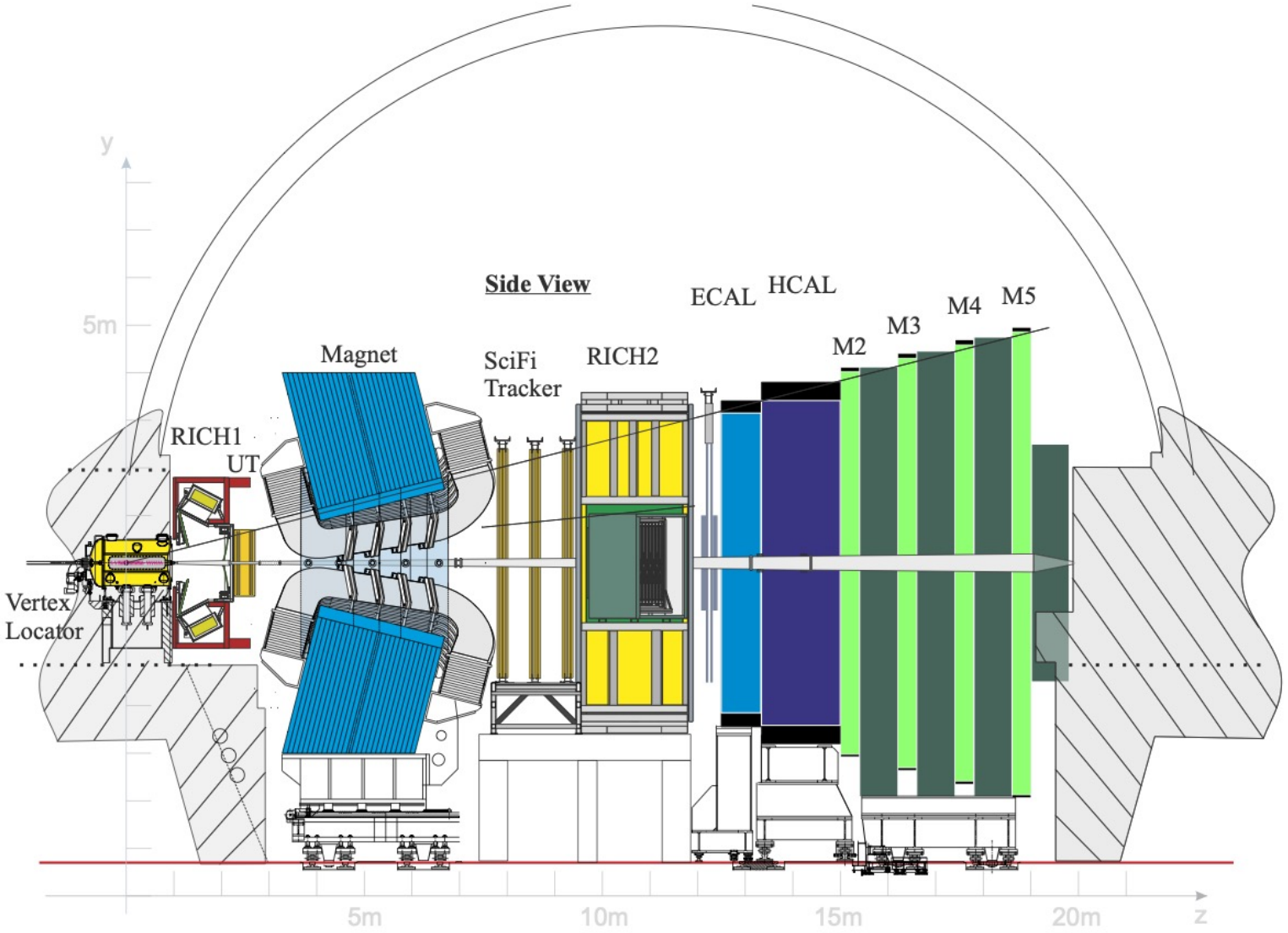

Figure 2.2: Schematic side view in the y-z plane of LHCb experiment inside the cavern.

2.2.1 Vertex Locator

The Vertex Locator (VELO) is the first sub-detector of the tracking system. Its main purpose is to detect tracks originated from the primary interaction point. The track reconstructed by the VELO are used as seed in the tracking procedure and are involved in the new full software trigger [18].

Since beauty and charmed hadrons usually travel few centimetres before decaying the VELO need to be able to reconstruct displaced decay vertices close to the primary vertex and have excellent impact parameter resolution. To do so it requires a micrometre resolution.

The VELO sub-detector should:

- have at least four hits for each track in LHCb acceptance;
- have the finest spatial resolution where the module is closest to the interaction point;
- be, along with the RF box, as close as possible to the interaction point;
- have minimal material budget in the fiducial region.

This sub-detector is composed of 52 modules arranged as in Fig. 2.3, distributed to ensure a full coverage of the pseudo rapidity acceptance of LHCb. The modules are mounted on two movable halves, Side C and Side A. Each side can move independently, and can retract, during beam commissioning, or extend up to 5.1 mm of distance of the active section from the beam line.

To separate the primary vacuum of the beam line from the secondary vacuum of the detector an RF box, composed of 250 µm thick aluminium, is placed inside the beam pipe.

To achieve the necessary resolution of momentum each module is composed of 55 µm$\times$ 55 µm pixels with a thickness of 200 µm.

The pattern recognition efficiency of the reconstruction track is defined as

$$\varepsilon_{\text{rec}} = \frac{N_{\text{reconstructed and reconstructible}}}{N_{\text{reconstructible}}}, \tag{2.1}$$

and simulations have shown excellent performances. The efficiency of reconstructed tracks was measured $\varepsilon_{\text{rec}} > 98.9\%$ up to $\varepsilon_{\text{rec}}99.8\%$ depending on the requirements on the tracks. Simulations have also shown a ten time smaller ghost rate with respect to the old VELO module at Run 3 conditions of luminosity and pile-up.

On the left of Fig. 2.4, it is possible to notice how the upgraded sub-detector has extremely high efficiency also for low transverse momentum tracks. On the right is possible to notice the increased resolution on the impact parameter. This is a fundamental parameter as in a lot of trigger strategy for different analysis.

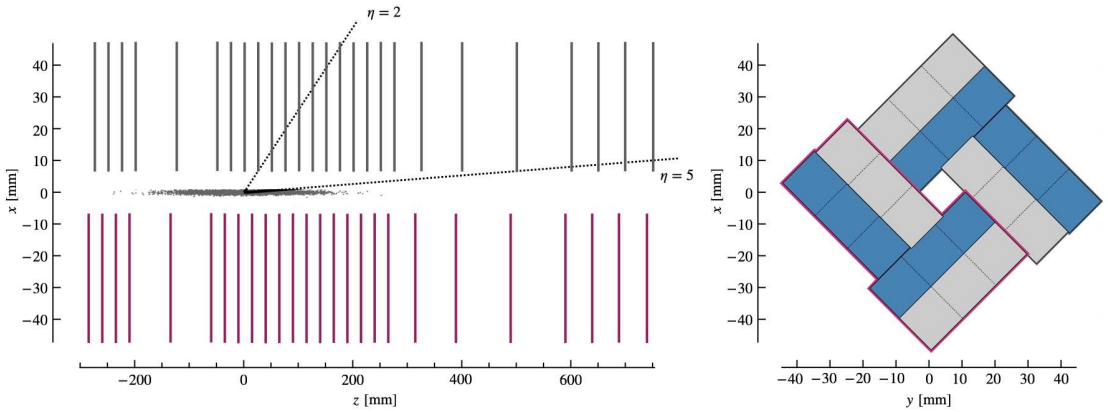

Figure 2.3: VELO Schematic. On the left it is shown in the x-z plane while on the right it is shown in the x-y plane. The side C is highlighted in purple colour.

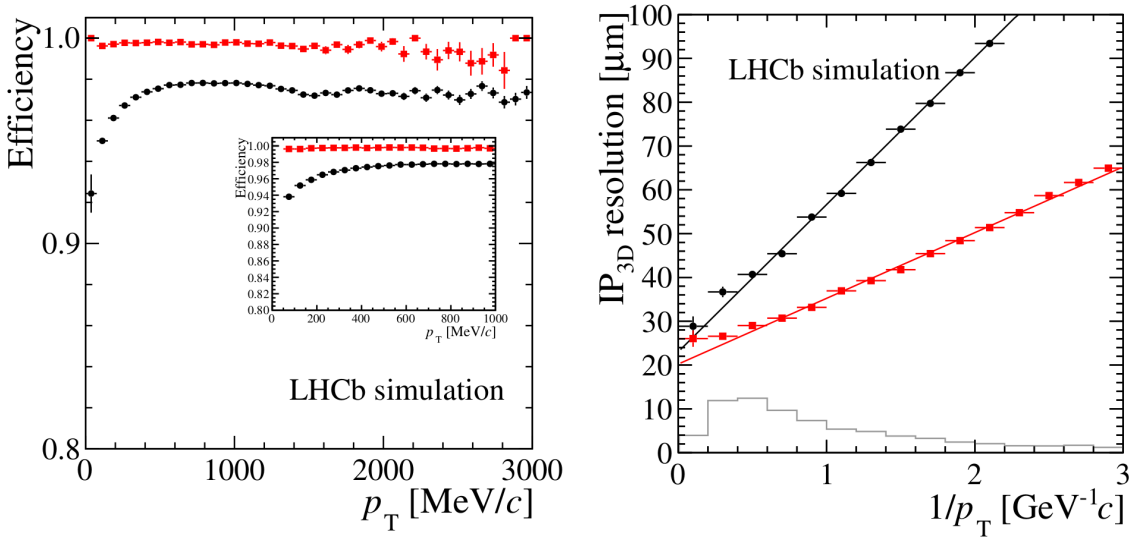

(a) Efficiency of reconstructed tracks

(b) Resolution on the impact parameter

Figure 2.4: On the left: efficiency of reconstruction for the VELO module as function of the transverse momentum of the tracks p_T at Run 3 conditions. On the right: resolution of the reconstructed impact parameter as function of transverse momentum p_T. In both plots, in black the old VELO sub-detector and in red the newly upgraded one.

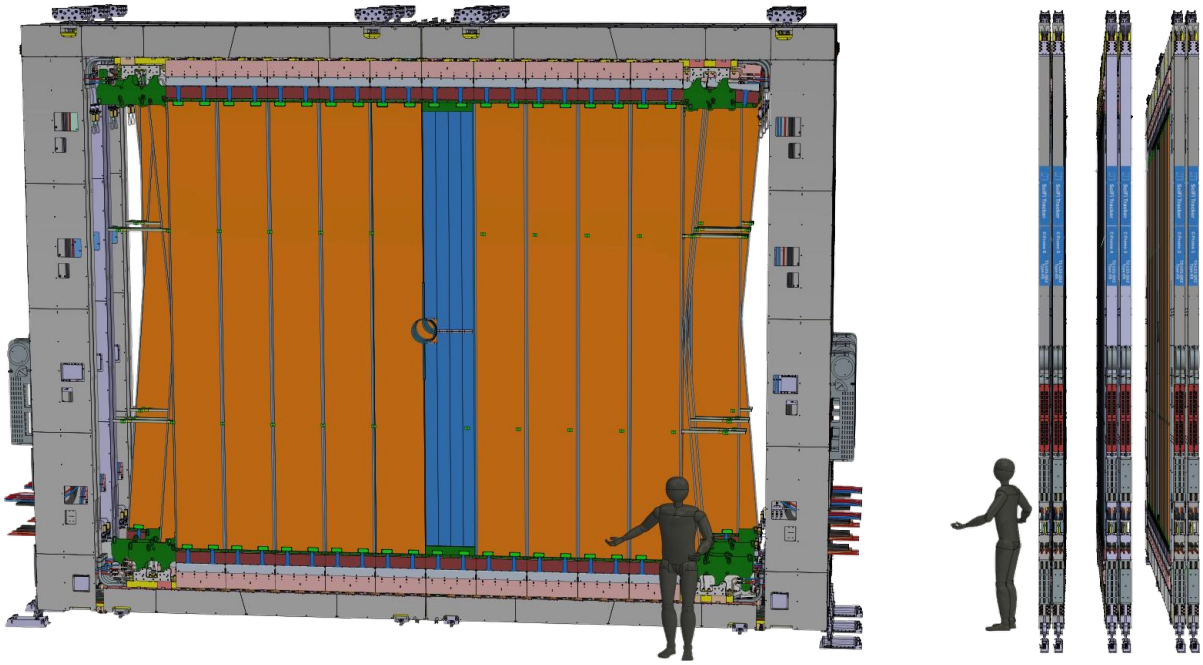

Figure 2.5: Drawing of the SciFi sub-detector. On the left, the view in the x-y plan, on the right, the view in the y-z plane. On the left in blue is possible to distinguish the various mats of scintillating fibres and in orange the module of the layer.

2.2.2 Scintillating Fibre Tracker

The scintillating fibre tracker (SciFi tracker) is the last element of the tracking system of LHCb.

It is composed of three independent station each composed of 4 layers of plastic scintillating fibres with a diameter of 250 µm arranged in multi-layer fibre mats for a total of 12 detection planes. The two central layer of each station are rotated by ± 5 ° to reconstruct the vertical position of the track. The signal of the scintillating fibres are read out by silicon photomultiplier (SiPM) placed on both ends [19].

Each layer is composed by ten, twelve for the last station, module each composed by eight $\sim$ 2.4 m long and $\sim$ 13 cm wide mats made of six layers of scintillating fibre. A precise calibration of these mats and its effect will be discussed in details later in Sec. 3.2.

The main requirements for the new SciFi detector are

- the hit detection efficiency should be maximized while the noise due to wrong reconstructed clusters should be minimized;
- the resolution on the single hit on the x-axis, i.e. the bending plane, must be < 100 µm. This detector does not require a higher resolution as the main constraint

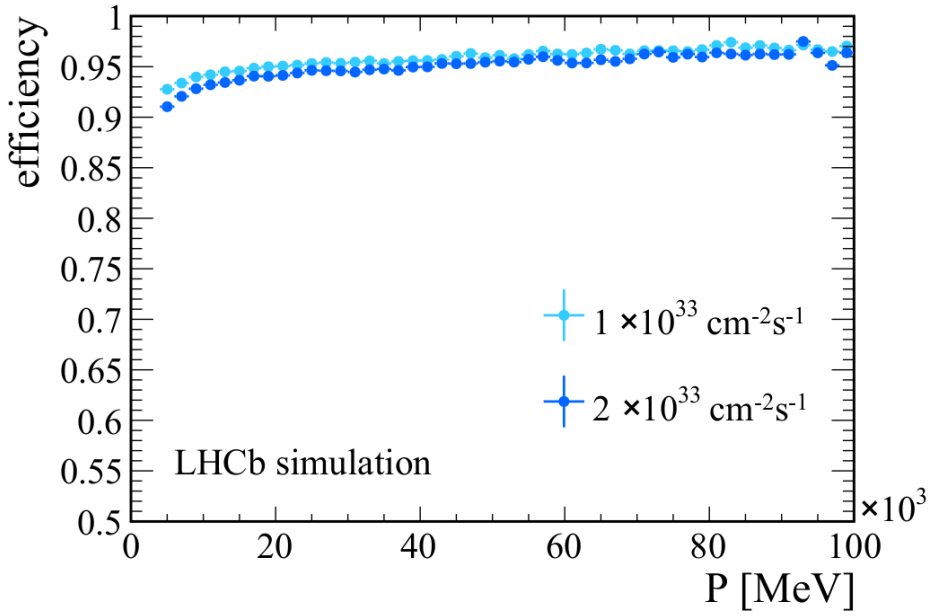

Figure 2.6: Tracking efficiency for long tracks in function of the momentum of the tracks reconstructed with the new tracking algorithm.

in extrapolating the tracks from the VELO are dominated by multiple coulomb scattering;

- to minimize the multiple coulomb scattering effect of the detector itself the total radiation length X of each detector layer should be $X/X_0 \leq 1\%$;
- to account for the new condition of Run 3 it should operate with these performances for a luminosity of up to 50 fb and it should be read out at a frequency of 40 MHz.

Simulations have shown that the SciFi tracker, along with the others tracking sub-detector, greatly improve the performance of the tracking algorithm. It was shown that for the conditions of Run 3 the new tracking system has $2 - 4\%$ less efficiency of the efficiency of the old detector in 2011 condition, i.e. with less luminosity and less pile-up.

In Fig. 2.6 it is reported the efficiency of the tracking algorithms used to reconstruct long track (see Sec. 2.4.1) in Run 3 conditions.

2.3 Particle Identification Systems

The particle identification system (PID) allows distinguishing between different system and is of fundamental importance for LHCb. It is composed of two Ring Imaging

Cherenkov detectors (RICH1 and RICH2), an electromagnetic calorimeter (ECAL) a hadron calorimeter (HCAL) and the muon system.

RICH detectors are particularly important in the separation of pions and kaons, that results fundamental in CP violation studies.

On the other hand calorimeters are mainly focused on electron and photon identification

As shown in Fig. 2.2, the RICH1 is placed before the magnet while the RICH2 and the ECAL and HCAL are placed between the SciFi and the muon stations. The radiator of RICH1, C_4F_{10} at standard pressure and temperature, has a refractor index $n = 1.0014$ and allows to PID particle with momentum between 2.6 and 60 GeV/c. RICH2 is designed to provide PID for higher momentum particle, i.e. between 15 and 100 GeV/c. To do so it uses CF_4 as radiator with a refractive index of $n = 1.0005$ [20]. For both RICH detectors the whole photon detector chain has been replaced in Upgrade 1 to account for the new 40 MHz read-out frequency to cope with the increased occupancy of RICH detectors.

In Fig. 2.7 the two RICH detectors are shown. RICH1 covers an acceptance of $25 - 300$ mrad in the magnet bending plane and of $25-250$ mrad in the vertical plane. RICH2 covers an acceptance of $15 - 120$ mrad in the magnet bending plane ad $15 - 100$ mrad in the vertical plane. In both detectors the light produced by the radiator is deflected using mirrors outside the LHCb acceptance to be read-out by Multi Anode PMTs. Since they are placed outside the LHCb acceptance regions the magnetic field has negligible effects on the PMTs.

In the calorimeter system from Run1-2 the Scintillating Pad Detector (SPD) and the PreShower (PS) sub-detectors have been removed while the overall layout of ECAL and HCAL have been left unmodified.

ECAL is a shashlik calorimeter composed of 66 lead layers 2 mm thick alternated with scintillating layers 4 mm thick for a total of 25 radiation length of thickness. This is needed to ensure a complete shower containment for high energy particle and provide the necessary energy resolution. On the transverse plane it is segmented in three regions: inner, middle and outer section with increasing area of sensitivity from the beam pipe outwards. It was designed to provide uniform resolution on $E \sin\theta$ for each cell, in which θ is the angle of the vector pointing to the cell from the interaction point. A single cell of the outer section is present in Fig. 2.8. The energy resolution of the calorimeter is parametrized as

$$\frac{\sigma(E)}{E} = \frac{(9.0 \pm 0.5)\%}{\sqrt{E}} \oplus (0.8 \pm 0.2)\% \oplus \frac{0.003}{E \sin\theta}, \tag{2.2}$$

where E is the energy expressed in GeV and θ has been previously defined.These parameters have been measured thanks to an electron test beam.

HCAL is a hadronic sampling calorimeter composed of iron and plastic scintillator for a total thickness of 5.6 interaction lengths since the full containment of hadronic showers

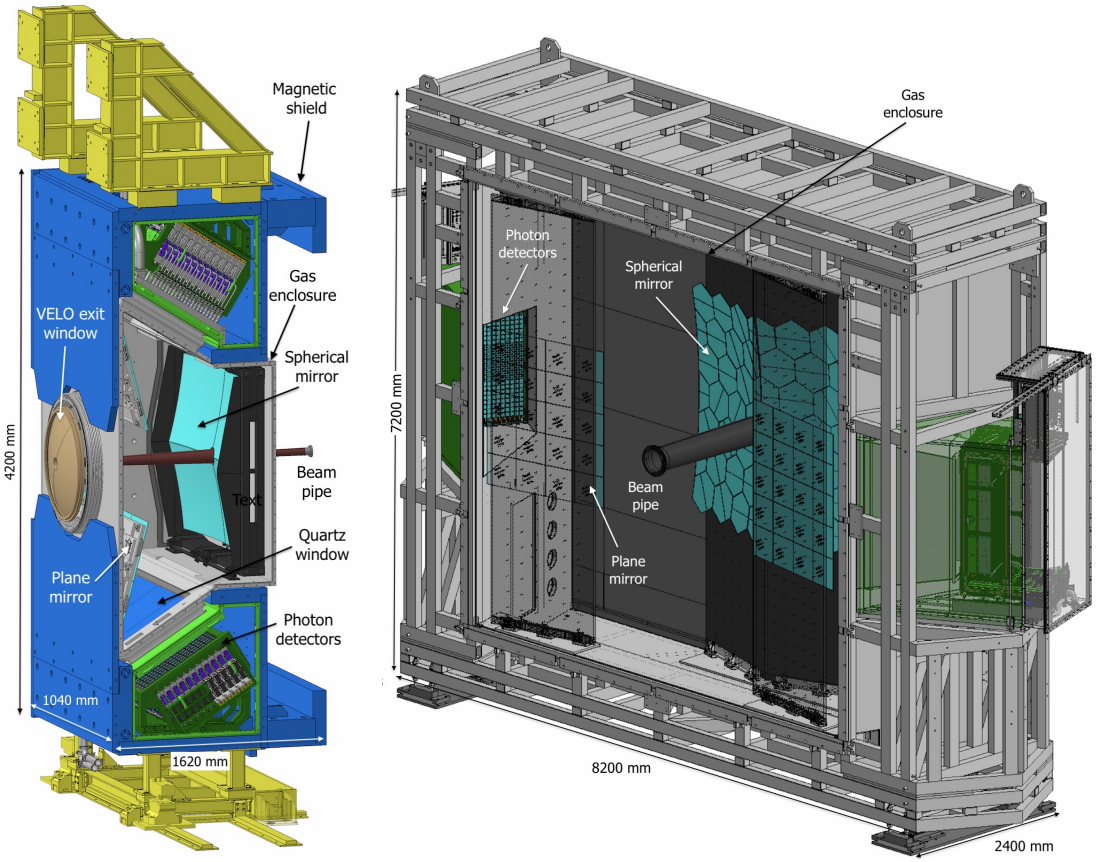

(a) RICH1 (b) RICH2

Figure 2.7: Rendering of the two RICH detectors, on the left RICH1 and on the right RICH2.

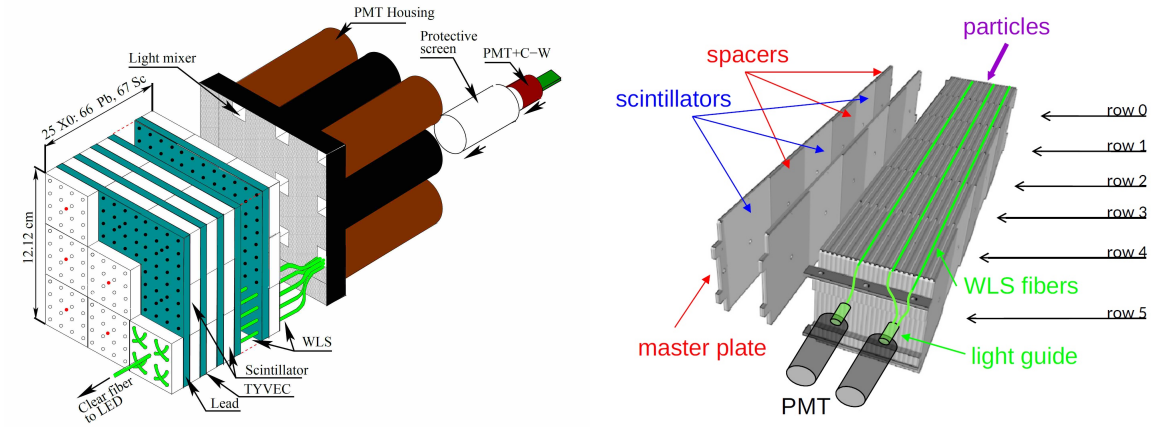

(a) ECAL cell

(b) HCAL cell

Figure 2.8: Schematics for ECAL and HCAL single cells.

is not a strict requirement for the energy resolution and the identification of hadrons. On the transverse the HCAL is only segmented in two regions, inner and outer, with a larger granularity with respect to the ECAL due to the different characteristic of hadronic showers from electromagnetic showers. The energy resolution of the HCAL is parametrized as

$$\frac{\sigma(E)}{E} = \frac{(67.5 \pm 5)\%}{\sqrt{E}} \oplus (9 \pm 2)\%, \tag{2.3}$$

where E is the energy deposited in GeV. A single cell of the HCAL is also present in Fig. 2.8.

2.4 Trigger System and Data Acquisition

LHCb in Run 3 is adopting a trigger-less readout system and a full software trigger. During Run 1-2 one of the main limitation for production asymmetry measurement and for statistics in general, was introduced by the Level-0 trigger that reduced the readout to 1 MHz [13]. This trigger was the largest source of inefficiency at the trigger level and for the Upgrade 1 has been removed. Instead, LHCb is now using a full software trigger reconstructing events at $\sim$ 30 MHz, with a readout electronics that are able to reach a frequency of readout of 40 MHz [21]. Due to the high similarity of signal and background events it is not possible to employ a traditional inclusive trigger strategy in which signals are identified with a small set of signatures. For this reason LHCb has introduced, during Run 2, the real-time analysis approach in which the trigger performs a full offline-quality reconstruction thank to quasi-real-time alignment and calibration. In order to do so the trigger system is dived in two stages: High Level Trigger 1 (HLT1)

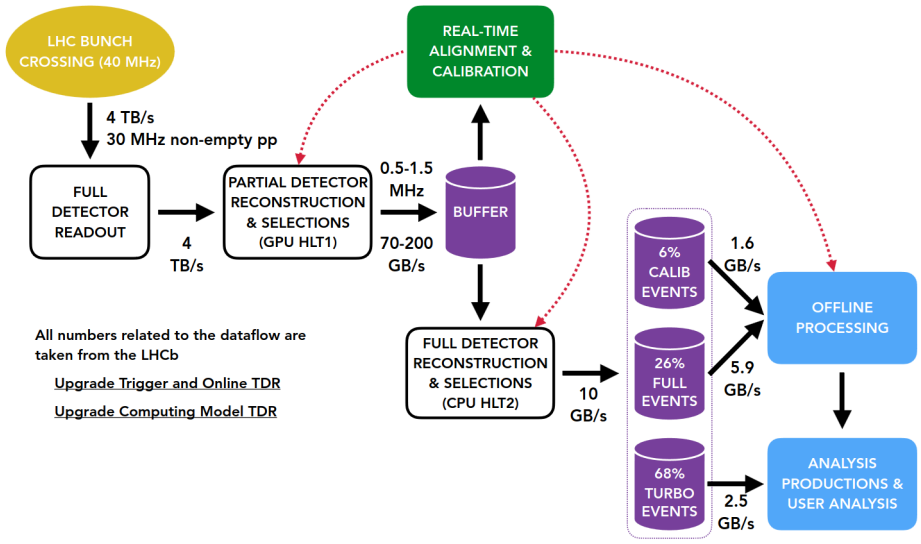

Figure 2.9: Dataflow of the Run 3 full-software, full-readout trigger system and data acquisition system[22].

based on the partial reconstruction of charged particles and High Level Trigger 2 (HLT2) that perform the full event reconstruction and selection of signal candidates.

The HLT1 goal is to lower the event rate allowing the data to be buffered on disk for real-time alignment, calibration, and subsequent processing in HLT2, all while ensuring a high level of efficiency throughout the LHCb physics program. Charm hadrons are present in almost 1 MHz events while beauty hadrons are present in 300 kHz events. The frequency from other physics topics of LHCb are significantly lower except for strange hadrons. These are produced with a higher frequency of charm hadrons but are not in the main scopes of LHCb, so it is given preference to rare strange decays [21].

To cover this physics program an estimated maximum output of HLT1 of 2 MHz at a luminosity of $\mathcal{L} = 2 \times 10^{33}$ cm^{-2}s^{-1} should provide enough statistics. On the other hand, if there is a very high collider efficiency, it is possible to reduce the output frequency of HLT1 up to 500 kHz, to prevent overflowing the buffer while remaining efficient in the charm physics channels.

HLT2 should support $\sim$ 1000 independent selections for signals using the full offline-quality reconstruction with offline-quality alignment and calibration. In Fig. 2.9 a schematic of the dataflow in LHCb.

2.4.1 High Level Triggers and different modalities

HLT1 focuses on tracks of charged particles generated within the VELO that also have hits on other tracking sub-detector (e.g. SciFi, UT and muon stations). Before running

the HLT1 algorithm a global event cut is applied, excluding a fraction of events with a very high number of tracks due to high computational needs. HLT1 must be able to reconstruct and select these signatures

- tracks vertices displaced from the primary vertex, since this signature is typical of many LHCb analysis;
- leptons, particularly muons, independently of the displacement from the primary vertex, that are useful for many others LHCb analysis.

To recognize these signatures HLT1 must be able to

- reconstruct all tracks in the VELO sub-detector acceptance, to reconstruct the primary vertex, in order to measure the eventual displacement of tracks to distinguish between displaced and non-displaced tracks;
- reconstruct tracks outside the VELO regardless if they are displaced or non-displaced;
- reconstruct track momentum at the percent level;
- provide an accurate and precise covariance matrix of the measurements for particle tracks close to the beam pipe;
- distinguish between muons and non-muons tracks.

The algorithm of HLT1 is structured as follows: primary vertices are reconstructed thanks to tracks in the VELO. These tracks are then extrapolated to other tracking sub-detector (UT, SciFi), using a parametrization of the magnetic field and a minimum allowed transverse momentum. Above this minimum threshold the transverse momentum is already known with a percent-level precision and is then used as input parameter in a simplified Kalman Filter that estimate position and covariance matrix of the particle at the beam line. In this way, HLT1 can measure IP and displacements from the primary vertices with similar precision to HLT2. Lastly it distinguishes between muon and non-moun tracks and fit tracks to a common origin to form two-tracks displaced vertex candidates. Then based on all this information HLT1 applies the required selection.

HLT2 perform first an offline-quality reconstruction and then applies its selection algorithm to choose which events to be recorded to permanent storage. HLT2 reconstruction is based on four main components: charged particle pattern recognition, calorimeter reconstruction, particle identification and a Kalman fit of reconstructed tracks.

During charged particle pattern recognition, different algorithms allow rebuilding different tracks topology. Tracks rebuilt by HLT2 can be distinguished in *velo tracks*, *upstream tracks*, *downstream tracks*, *T tracks* and *long tracks* as shown in Fig. 2.10. VELO tracks are used to determine the main interaction point of the proton-proton collision. Knowing both the primary vertices and tracks trajectories allows identifying

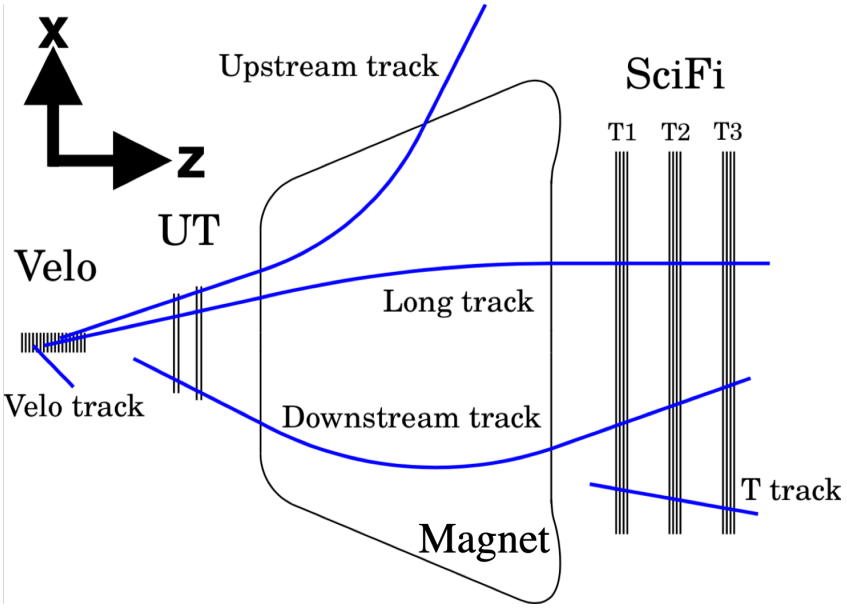

Figure 2.10: Nomenclature of possible tracks reconstructed by HLT2.

displaced tracks. Long tracks are the most used in LHCb analyses since they have the best moment resolution.

To best estimate the parameters of each track with maximum accuracy and precision a fit using a Kalman filter approach, called Kalman fit, is performed. After this step, ECAL hits are reconstructed during calorimeter reconstruction, allowing to discriminate between single photon hits, multiple photon hits and electrons. With this information, along with RICHs information and muon system data, long-lived particle (i.e. pions, kaons, protons, electrons and muons) are identified during particle identification for which a precise knowledge of the trajectory is fundamental.

After these steps, HLT2 applies $\mathcal{O}(1000)$ selections, each tuned for a particular signal topology or physical analysis, and data are stored permanently.

An important note for the subsequent analysis is distinguishing events with Trigger On Signal (TOS) and events with Trigger Independent of Signal (TIS). In the first case the signal candidate are the ones which triggered the event while in the TIS case something else is present in the event that has a disjointed set of detector hits and that triggered the event itself. Distinguishing between these two category of signal candidates can help better understand reconstruction and trigger effects on the signal itself. This distinction will be investigated further in Sec. 3.3.1.

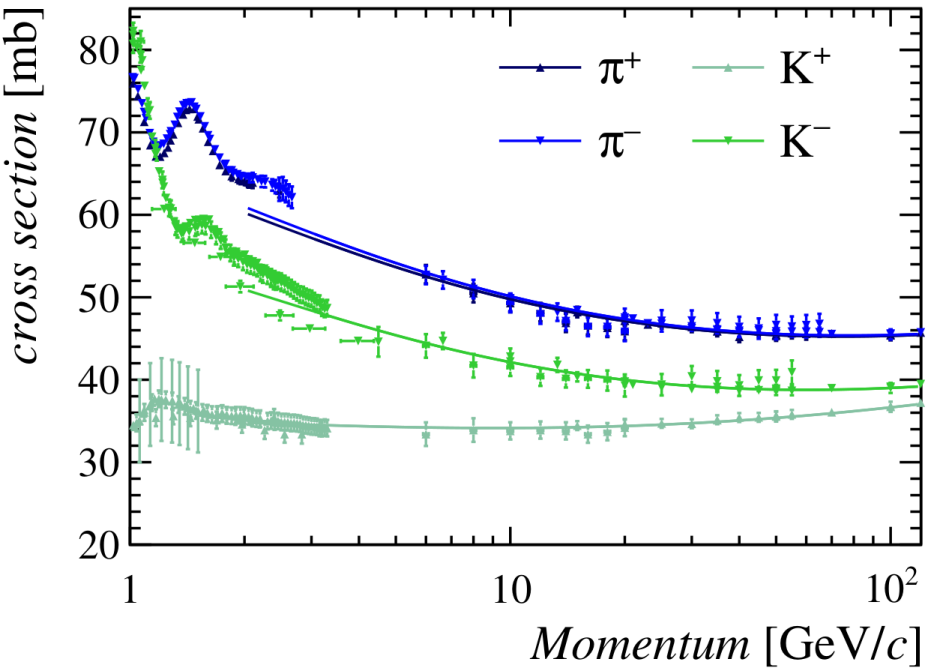

Figure 2.11: Total cross-section for charged pions and kaons on a target of deuterium, in function of their momentum. It is clearly visible that, at low momentum there is a charge asymmetry for charged kaons.

2.5 Detector Induced Asymmetries

Measure of CP asymmetries are reaching higher and higher precision at LHCb, along with useful measure of production asymmetries [23]. A lot of different analysis in these directions are prone to systematic effects due to the detector itself that may bias the results. These effects include, for example, material interaction of particles with the detector and difference in the reconstruction of tracks. In particular, it is known that kaon interactions with the material of detectors are subject to a charge-asymmetry effect as shown in Fig. 2.11, in particular for low momentum. This kind of effects introduce a difference in the kaons' detection efficiency. The precision of the measure involving kaons can therefore be influenced by these effects. For these reasons it is important to properly estimate these asymmetries for high precision measures such as CP violation measure in $D^0 \to K^-K^+$ and $D^0 \to \pi^-\pi^+$ [24].

Rather than the single particle detection asymmetry, it was found easier to access the combined asymmetry of kaons and pions $A^{\text{det}}(K^-\pi^+)$ rather than of the kaon alone. This can be defined as

$$A^{\text{det}}(K^-\pi^+) = \frac{\varepsilon^{\text{det}}(K^-\pi^+) - \varepsilon^{\text{det}}(K^+\pi^-)}{\varepsilon^{\text{det}}(K^-\pi^+) + \varepsilon^{\text{det}}(K^+\pi^-)}, \tag{2.4}$$

with ε^{det} the absolute detection efficiency of the $K\pi$ pair.

This measure was already performed in Run 2 in bins of the kaon momentum, and was found to be $A^{\text{det}}(K^-\pi^+) = (-0.89 \pm 0.15 \pm 0.06)$ and $A^{\text{det}}(K^-\pi^+) = (-1.03 \pm 0.06 \pm 0.06)$ respectively in 2015 and in 2016 [23]. The experimental methodology to extract this quantity will be discussed in the following Chapter.

Chapter 3

Estimation of Detection Asymmetries at LHCb

In this Chapter I will present the results of the analysis to estimate detection asymmetries at LHCb. These analyses have been carried out with different tools such as ROOT [25], and LHCb software.

In Sec. 3.1, I will present the main goals of this analysis effort and the strategy to extract the detection asymmetry. In Sec. 3.2, I will discuss some preliminary studies that have helped better understand the detector and are a starting point for the following analysis of detection asymmetries. In Sec. 3.3, I will explain how the data sample for the full analysis have been selected through additional studies. In Sec. 3.4, I will present different methods that were applied to perform the re-weighting, pros and cons for each method and the one I have used in the final analysis. In Sec. 3.5, I will discuss the fit method used in the final analysis and the measure for the detection asymmetry. In Sec. 3.6, I will show some additional studies for the validation of the fit and the estimation of the uncertainty of the measure. Lastly, in Sec. 3.7, I will summarize the main result of these studies presented in this chapter and I will discuss them in view of possible future applications.

3.1 Production Asymmetry and Analysis Strategy

The final goal of this analysis effort is to measure production asymmetries of D mesons in function of their kinematics, i.e. pseudo-rapidity η and transverse momentum p_T. This is a very useful measure as it can be used as input parameter in studies for non-perturbative QCD simulations and for high precision CP asymmetry measurements.

Detection asymmetries are a fundamental input parameter for production asymmetries measurement. In particular, to obtain the production asymmetry of D^0, $A^{\text{prod}}(D^0)$,

the measurement of $A^{\text{det}}(K^-\pi^+)$ is necessary. Namely,

$$A^{\text{prod}}(D^0) = A^{\text{raw}}(D^0 \to K^-\pi^+) - A^{\text{det}}(K^-\pi^+), \tag{3.1}$$

with $A^{\text{raw}}(i \to f)$ defined as

$$A^{\text{raw}}(i \to f) = \frac{N(i \to f) - N(\bar{i} \to \bar{f})}{N(i \to f) + N(\bar{i} \to \bar{f})}, \tag{3.2}$$

with $N(i \to f)$ the number of observed decay of a particle i to the final state f and $A^{\text{det}}(K^-\pi^+)$ defined as

$$A^{\text{det}}(K^-\pi^+) = \frac{\varepsilon^{\text{det}}(K^-\pi^+) - \varepsilon^{\text{det}}(K^+\pi^-)}{\varepsilon^{\text{det}}(K^-\pi^+) + \varepsilon^{\text{det}}(K^+\pi^-)}, \tag{3.3}$$

with $\varepsilon^{\text{det}}(K^-\pi^+)$ the absolute detection efficiency of the $K\pi$ pair.

The chosen decay to extract the detection asymmetry of the $K\pi$ pair are $D^+ \to K^-\pi^+\pi^+$ and $D^+ \to \overline{K}^0\pi^+$ with $\overline{K}^0 \to \pi^+\pi^-$. These are Cabibbo favoured decays with CP violation expected to be well below 10^{-4}.

Their raw asymmetry can be decomposed in [23]

$$A^{\text{raw}}(D^+ \to K^-\pi^+\pi^+) = A^{\text{det}}(K^-\pi^+) + A^{\text{det}}(\pi^+) + A^{\text{prod}}(D^+) + A^{\text{trigger}}, \tag{3.4}$$

$$A^{\text{raw}}(D^+ \to \overline{K}^0\pi^+) = A(\overline{K}^0) + A^{\text{det}}(\pi^+) + A^{\text{prod}}(D^+) + A^{\text{trigger}}, \tag{3.5}$$

with $A^{\text{det}}(\pi^+)$ the detection asymmetry induced by pions, A^{trigger} the charge asymmetry introduced by the trigger and $A(\overline{K}^0)$ the asymmetry introduced by CP violation in the neutral kaon system.

To extract the $A^{\text{det}}(K^-\pi^+)$, Eq. 3.5 can be subtracted from Eq. 3.4 to eliminate all other possible asymmetries. This leads to

$$A^{\text{det}}(K^-\pi^+) = A^{\text{raw}}(D^+ \to K^-\pi^+\pi^+) - A^{\text{raw}}(D^+ \to \overline{K}^0\pi^+) - A(\overline{K}^0). \tag{3.6}$$

Both $A^{\text{raw}}(D^+ \to K^-\pi^+\pi^+)$ and $A^{\text{raw}}(D^+ \to \overline{K}^0\pi^+)$ will be determined via a simultaneous fit.

As a first step the background in the sample is reduced both with fiducial cuts and the s-Plot technique to create the kinematic distribution for the next step as will be described in Sec. 3.3.2.

Since both $A^{\text{det}}(\pi^+)$ and $A^{\text{prod}}(D^+)$ depend on the kinematic of the referring particle, to ensure a proper cancellation in Eq. 3.6 kinematics weights are assigned to each event before the simultaneous fit. This ensures the kinematic distribution of both the D meson and the pion to be compatible between the two decay modes. More details of this procedure are given in Sec. 3.4.1.

Variable	Cuts
$p_T(D^{\pm})$	> 2500 MeV
IP($D\pm$)	< 0.1 mm
$\eta(D\pm)$	< 3.8

Table 3.1: Fiducial cuts applied to the sample of 2022 data with the V9 alignment and run number of the dataset.

3.2 Early Measurements of Run 3 and Alignment Effect

The detection asymmetry of the $K\pi$ pair is measured analysing analysed Run 3 data collected by LHCb during the 2022 data taking campaign. These data were relatively new are used to study misalignment effects.

As a first check, the $D^+ \to K^-\pi^+\pi^+$ sample is analysed. A series of fiducial kinematic cuts were applied to reduce the background. These cuts were chosen looking at the comparison of the sideband distribution, i.e. mainly background, and the subtraction between the mass peak region and the sideband region, i.e. mainly signal. They are reported in Tab. 3.1. They consist in the transverse momentum p_T, the pseudo-rapidity η and the impact parameter IP of the D meson. The data obtained from LHCb have been processed using the most recent alignment available ate the time, the V9 alignment. The data sample have been split in two subset depending on the polarity of the magnet, i.e. magnet up polarity with the magnetic field oriented as the positive y-axis and magnet down polarity with the magnetic field oriented as the negative y-axis.

In Fig. 3.1 the invariant mass distribution of D^+ and D^- are reported for magnet down configuration. The two distribution are simultaneously fitted with the following extended model

$$\begin{aligned} N_{bckg} + \frac{1}{2}N_{sig}[&(1+A_{raw})(f^+_{sig}G^+(\mu^+_1,\sigma^+_1) + (1-f^+_{sig})CB^+(\mu^+_2,\sigma_2,\alpha^+,n^+)) \\ &+(1-A_{raw})(f^-_{sig}G^-(\mu^-_1,\sigma^-_1) + (1-f^-_{sig})CB^-(\mu^-_2,\sigma_2,\alpha^-,n^-))], \end{aligned} \tag{3.7}$$

with N_{bckg}, N_{sig} the signal yields for background and signal, G^+, G^- are Gaussians for D^+ and D^- signal, CB^+, CB^- are Crystall Ball functions, f^+_{sig}, f^-_{sig} are the fraction of signal of each of these two function, and A_{raw} is the raw asymmetry of the sample. The crystal ball function has been chosen to represent the non-symmetric behaviour of the tails of the distributions. The distributions are centred around $\mu^+ = (1862.4 \pm 0.2)$ MeV for D^+ and around $\mu^- = (1877.6 \pm 0.2)$ MeV for D^-. These two values are incompatible with the real mass of the $D^{\pm}$ meson as $m^+ = m^- = (1869.66 \pm 0.05)$ MeV[5]. This behaviour hints to a wrong momentum estimate of the daughter particles before the invariant mass is calculated.

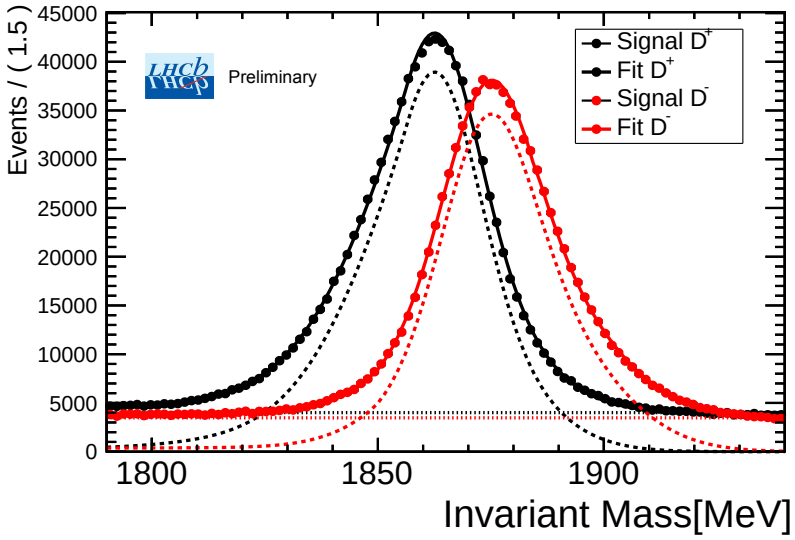

Figure 3.1: Invariant mass distribution for D^+, in black, and D^-, in red, with magnet down configuration and V9 alignment from $D^+ \to K^-\pi^+\pi^+$. In the solid line the fitted function to the distribution.

To provide an estimate of how important this effect is, a simple shift is applied to the momentum of the daughter particles. The shift is parametrized as

$$p_{\text{new}} = (1 + \alpha)p_{\text{old}}, \tag{3.8}$$

with the sign α that depends on the charge of the particle.

The resulting distributions are reported in Fig. 3.2 in green and blue along with the other distributions of Fig. 3.1. The shift applied to the momentum is indeed able to partially correct the mean of the distributions with $\mu_s^+ = (1867.7 \pm 0.1)$ MeV and $\mu_s^- = (1870.8 \pm 0.3)$ MeV, much closer to the real value of the $D^\pm$ meson. These value have been obtained with a shift of $\alpha = \pm 0.072$. The model of the fit for the shifted distributions has been slightly changed with respect to the model for the non-shifted one, due to a slightly different shape of the distributions.

These differences in value of the invariant mass has been later found out to be due to a misalignment effect in the SciFi sub-detector. In particular, the V9 alignment included the precise position of each module of the SciFi but not of each mat individually. A later version of the alignment, the V9+MATS, partially solved this issued and greatly helped to reduce this shift in the mesons mass.

Along with this new alignment a validation of the data in the different runs helped exclude runs with various issues such as bad real-time calibration of VELO sub-detector or in the real-time calibration of the SciFi sub-detector. With this exclusion it was also

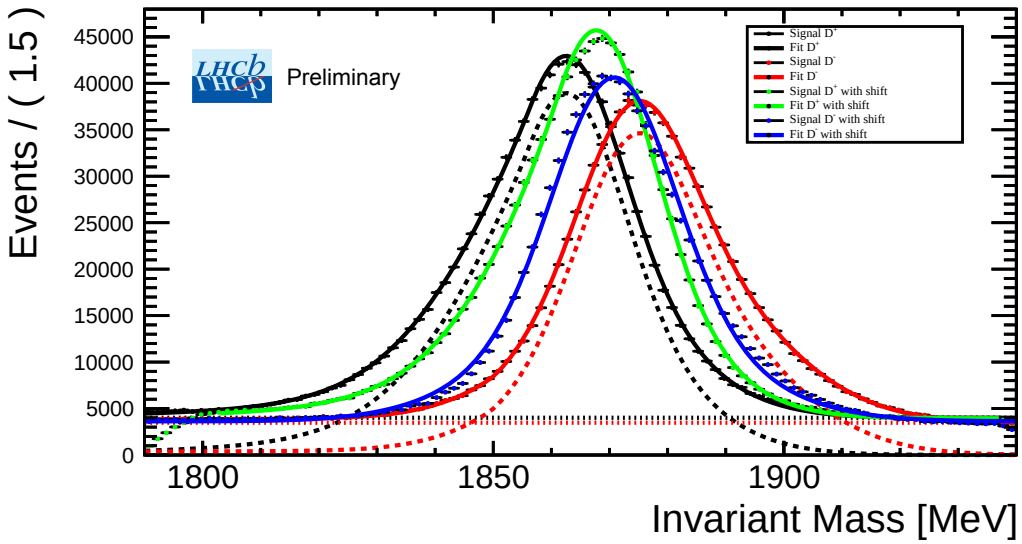

Figure 3.2: The invariant mass distribution for D^+, in black, and D^-, in red, overlapped with the shifted distribution for both D^+, green, and D^-, blue. These distributions are from $D^+ \to K^-\pi^+\pi^+$ decay mode, with magnet down polarity and V9 alignment.

Variable	Cuts
$p_T(D^\pm)$	> 2300 MeV
IP$(D\pm)$	< 0.1 mm
$\eta(D\pm)$	< 4.0

Table 3.2: New fiducial cuts applied to the sample of 2022 data with the V9+MATS alignment and run number of the dataset.

possible to loose the fiducial cut that are now reported in the Tab. 3.2 along with the correct run numbers.

The invariant mass distribution computed with this new alignment is reported in Fig. 3.3 for both polarities. The fit function has been changed so that μ_1 and μ_2 of Eq. 3.7 are now the same parameters. The new distributions for magnet down, after the simultaneous fit, are centred around $\mu^+ = (1867.773 \pm 0.008)$ MeV and $\mu^- = (1867.895 \pm 0.009)$ MeV. These values are now much closer to the real value of the $D^\pm$ meson mass, even if a slight shift is still present in particular for magnet up polarity. Looking at Fig. 3.3, it is possible to notice that the background have been greatly reduce thanks to this new alignment and the shape of the tails distributions is now more symmetric with respect to the old alignment. Comparing the signal yield between the two alignment it was also found an increase of +63% for magnet down polarity and +37% for magnet up polarity thanks to the new V9+MATS alignment.

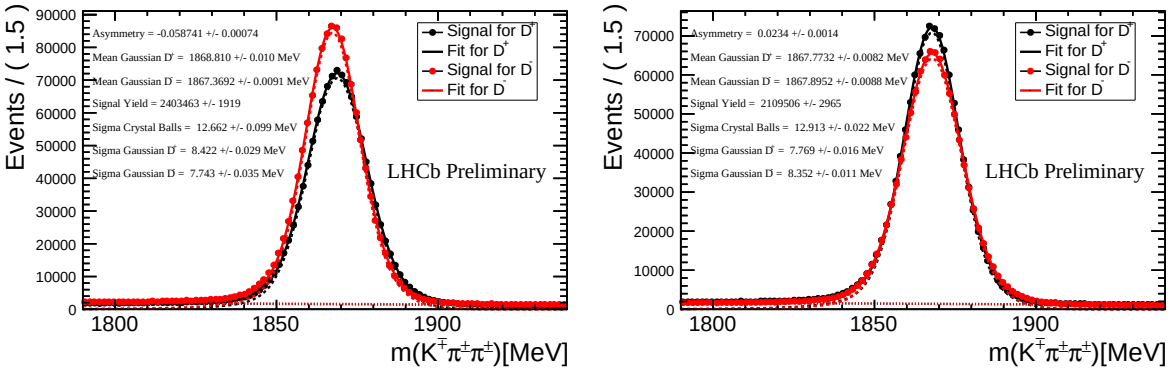

(a) Magnet up

(b) Magnet down

Figure 3.3: Invariant mass distribution of D^+ and D^- for magnet up polarity, on the left, and for magnet down polarity, on the right, for $D^+ \to K^-\pi^+\pi^+$ using the new V9+MATS alignment that reduced the displacement of mass peaks.

Furthermore, also the $D^+ \to K^0_s\pi^+$ has been studied with the same kinematic cuts of Tab. 3.2, with both the old V9 alignment and the new V9+MATS alignment. The resulting histograms are reported in Fig. 3.4. For V9 alignment is clearly visible a displacement of the mass peaks, at $\mu^+ = (1858.4 \pm 0.3)$ MeV for D^+ and $\mu^- = (1880.4 \pm 0.3)$ MeV for D^-, similar to what was found for $D^+ \to K^-\pi^+\pi^+$. Here, however the tails are even more asymmetric with respect to the asymmetric tails of Fig. 3.1. Once again, after applying the new V9+MATS alignment, it is clearly visible how the mass peaks are now overlapped, with the peak at $\mu^+ = (1867.72 \pm 0.13)$ MeV for D^+ and $\mu^- = (1868.23 \pm 0.14)$ MeV, much closer to the real value.

3.3 Data Sample Selection

In this section we will discuss how the dataset was chosen in the extraction of $A^{\text{det}}(K^-\pi^+)$. In particular, in Sec. 3.3.1 we will focus on the procedure that brought the decision on how to choose the dataset, while in Sec. 3.3.2 we will focus on the s-Plot technique employed to reduce the background in the kinematic distributions of each sample. Later on, these distributions will be the main focus of the kinematic reweighting to ensure the complete cancellation of additional asymmetries before extracting $A^{\text{det}}(K^-\pi^+)$.

3.3.1 Preliminary Analysis

As a first step, the fiducial cuts of Tab. 3.2 along with a filter on the run number were adopted. In addition, the trigger lines with the following requirement were asked.

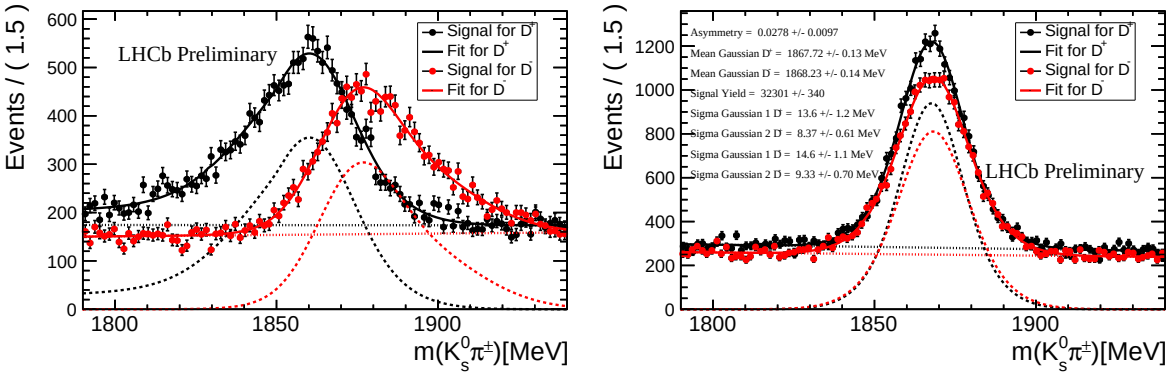

(a) V9 alignment

(b) V9+MATS alignemnt

Figure 3.4: Invariant mass of D^+, in black, and D^-, in red, for $D^+ \to K^0_s\pi^+$ in magnet down configuration. On the left with the V9 alignment where the mass peaks are displaced, on the right with the V9+MATS, where mass peaks are more overlapped.

- for TIS lines: the lines with most statistics for the D^+ meson for both $D^+ \to K^-\pi^+\pi^+$ and $D^+ \to K^0_s\pi^+$;
- for TOS lines: the lines with most statistics for the pion, either one present in $D^+ \to K^-\pi^+\pi^+$ or the bachelor pion of $D^+ \to K^0_s\pi^+$.

These requirements were made to already have a sample with a similar kinematic distribution in η, p_T for both D^+ and π^+. Other trigger lines were excluded: either were triggering on a particle not present in the other decay, e.g. the charged kaon, or were calibration lines, that would be rescaled in future data taking, or were highly inefficient. This was done to ensure the robustness of the analysis for future applications. The lines that were chosen are:

- for TIS lines: `Dp_Hlt1_Hlt1TwoTrackMVADecision_TIS`, a multivariate trigger that require two tracks and pick a decision based on the quality of the reconstructed impact parameter and the transverse momentum and `Dp_Hlt1_Hlt1TrackMVADecision_TIS`, similar to the precedent but only require one track. A logic OR of these two lines for both decay modes will be referred in the future as TIS sample.
- for TOS lines: `pip1_Hlt1_Hlt1TrackMVADecision_TOS`, the same trigger algorithm as before but applied on one of the pions of $D^+ \to K^-\pi^+\pi^+$ and as TOS instead of TIS and `hp_Hlt1_Hlt1TrackMVADecision_TOS`, that is applied to the bachelor pion of $D^+ \to K^0_s\pi^+$. In the future this will be referred as TOS sample.

Each of these samples were divided depending on the magnet polarity. In Fig. 3.5 the distribution of invariant mass in magnet down configuration have been reported for both

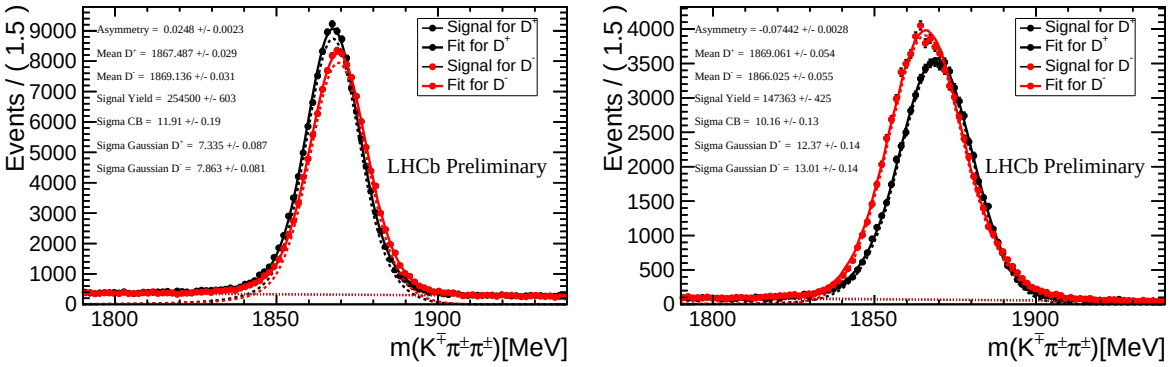

(a) TIS sample (b) TOS sample

Figure 3.5: Invariant mass distribution for $D^+ \to K^-\pi^+\pi^+$ for the TIS sample, on the left, and the TOS sample, on the right.

TIS and TOS sample. There are important difference in these samples, starting from the raw asymmetry. For the TIS sample was measured to be $A^{\rm raw}_{\rm TIS} = 0.025 \pm 0.002$ while for the TOS sample was measured to be $A^{\rm raw}_{\rm TOS} = -0.074 \pm 0.003$. This is due to the difference of the kinematics of the two samples, directly related to the raw asymmetry.Moreover, the TIS sample present more signal yield, but it is less pure with respect with the TOS sample that have a lower background. On the other hand the TOS sample present a wider mass peak.

This same behaviour was observed in the $D^+ \to K^0_s\pi^+$ sample as reported in Fig. 3.6. In these distributions the fit function has been changed to

$$N_{bckg}(a_0 + a_1 x) + \frac{1}{2}N_{sig}[(1 + A_{raw})(f^+_{sig}G^+_1(\mu^+, \sigma^+_1) + (1 - f^+_{sig})G^+_2(\mu^+, \sigma_2)) \\ +(1 - A_{raw})(f^-_{sig}G^-_1(\mu^-, \sigma^-_1) + (1 - f^-_{sig})G^-_2(\mu^-, \sigma_2))], \tag{3.9}$$

to account for a non-uniform background. The raw asymmetry has been found to be $A^{\rm raw}_{\rm TIS} = 0.021 \pm 0.026$ for the TIS sample and $A^{\rm raw}_{\rm TOS} = -0.042 \pm 0.015$ for the TOS sample.

The most relevant parameters measured during these preliminary analyses have been reported in Tab. 3.3 for all cases. The different behaviour for TIS and TOS samples is present in both magnet polarities with similar effects. Furthermore, here it is shown that the decay mode that will drive the uncertainty on $A^{\rm det}(K^-\pi^+)$ is the $D^+ \to K^0_s\pi^+$ due to its lower statistic with respect to the other decay mode.

The two sample have indeed very different behaviour due to the different trigger. This difference will be even more accentuated in the re-weighting step where the kinematic distributions will present important differences. So, from now on the two sample will be treated independently of each other. This is possible since the events that are shared in both sample are a negligible fraction, in particular in the $D^+ \to K^0_s\pi^+$ sample.

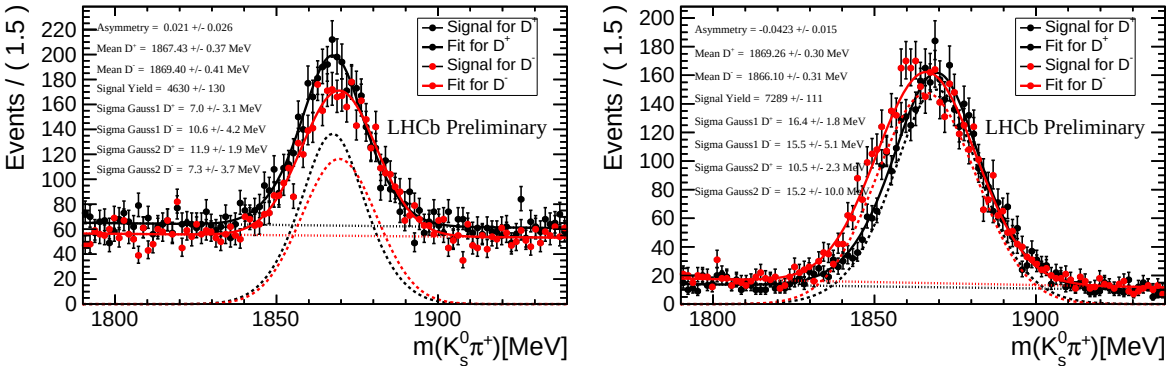

(a) TIS sample (b) TOS sample

Figure 3.6: Invariant mass distribution of $D^+ \to K^0_s\pi^+$ for TIS sample on the left and for TOS sample on the right. The TIS sample has notably more background with respect to the TOS sample.

Magnet Up	$D^+ \to K^-\pi^+\pi^+$	$D^+ \to K^0_s\pi^+$
TIS raw asymmetry	$-6.8 \pm 0.2\%$	$-7.0 \pm 2.2\%$
TIS signal yield	3×10^5	5.2×10^3
TOS raw asymmetry	$+5.2 \pm 0.2\%$	$+7.6 \pm 1.4\%$
TOS signal yield	1.6×10^5	7.2×10^3
Magnet Down	$D \to K\pi\pi$	$D \to K_s\pi$
TIS raw asymmetry	$+2.5 \pm 0.2\%$	$+2.1 \pm 2.6\%$
TIS signal yield	2.5×10^5	4.6×10^3
TOS raw asymmetry	$-7.4 \pm 0.3\%$	$-4.2 \pm 1.5\%$
TOS signal yield	1.5×10^5	7.2×10^3

Table 3.3: Most relevant results for the preliminary analysis for each decay mode, magnet polarity and trigger sample.

3.3.2 Background Reduction Technique

To have the signal distribution of the relevant kinematic distributions of both decay modes, we first need to subtract the background from the two samples before moving on to the re-weighting step. This is performed with the sPlot[26] technique after the preliminary fits of Sec. 3.3.1.

This technique consist in assigning a weight, from now on called *s-weight*, to each event based on the invariant mass function fitted to the distribution. To each event, the probability that the event belong to the signal or to the background is computed. From these probabilities we can assign an s-weight for both species of events (signal, background) from which we can then reconstruct additional distributions, such as the kinematic distributions so that the reconstructed distributions will be more pure in the respective species.

We are interested in the signal events, and so we will focus on computing s-weights for this species. These will be negative for events that are likely to be background event, i.e. events in the sideband region of the invariant mass, and be positive on events that are likely to be signal event, i.e. events in the mass peak region. The implementation used in this analysis work is based on RooStats environment in ROOT, `RooStats::SPlot` class [25]. These s-weights are computed for each sample, each magnet polarity and each decay mode independently, from the maximum likelihood fits of Fig. 3.5-3.6 and for magnet up polarity.

As an example, in Fig. 3.7, is reported the signal s-weights scatter plot in function of the invariant mass for one case. Here it can be noted how the events in the mass peak region have s-weights ~ 1 while events in the sideband region have negative value due to the high probability of being background events.

3.4 Re-Weighting Strategy

In this section we will discuss different re-weighting techniques that were applied to the data set to ensure the proper elimination of possible additional asymmetries as discussed in Sec. 3.1 before extracting the detection asymmetry.

For brevity, the decay mode $D^+ \to K^-\pi^+\pi^+$ will be referred to as $K\pi\pi$ and the $D^+ \to K^0_s\pi^+$ decay as $K_s\pi$. Since the decay mode $K\pi\pi$ has more statistics and signal yield than $K_s\pi$, it is the natural choice to re-weight the $K\pi\pi$ mode on the $K_s\pi$, to minimize the loss of statistics in the re-weighting process.

The s-weights for the signal, described in the previous section are applied to the kinematic distributions before any additional re-weighting.

In Fig. 3.8 are reported the distributions for D^+ and π^+ kinematics in the different samples that will be studied in this Section. In particular, we will focus on the transverse momentum and pseudo-rapidity of both D^+ and π^+. In Fig. 3.8a-3.8f are reported the

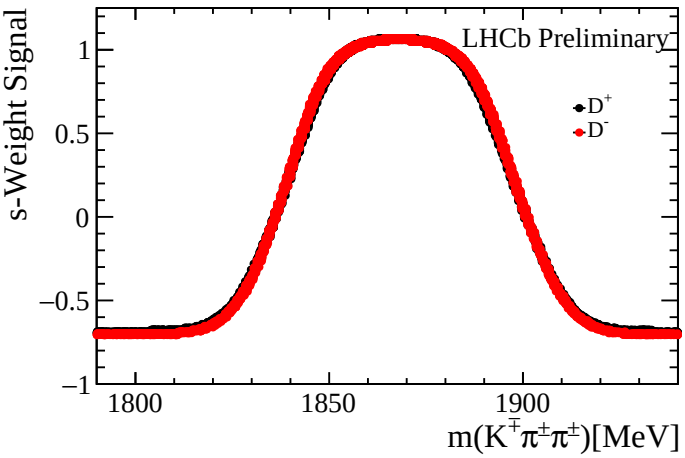

Figure 3.7: Scatter plot for s-weights for signal events in function of the invariant mass for $D^+ \to K^-\pi^+\pi^+$ decay mode, TIS sample and magnet down polarity as an example.

distributions for D^+, while in Fig. 3.8g-3.8l the ones for π^+. It is possible to observe that the TIS and TOS sample have quite different distributions, in particular for the p_T distribution. The TIS and TOS triggers have different thresholds on the p_T of the particle.

Since kinematic weights are not limited, the signal yield obtained after the weighting procedure of this section might be larger than the unweighted sample. Overall weights should not increase the statistical power of the sample, as they do not add statistics to the sample. To account for this, in this section weights will be renormalized with

$$w_{\text{eff}} = \frac{\sum_i w_i}{\sum_i w_i^2}, \tag{3.10}$$

where the sum is performed for each event in the sample and w_i is the weight of a single event. The effective total number of events N_{eff} then becomes

$$N_{\text{eff}} = w_{\text{eff}} \sum_i w_i, \tag{3.11}$$

so that $N_{\text{eff}} \leq N$ for every possible weights' distribution. However, with this normalization we expect a loss of statistical power that will be reflected in the estimation of uncertainty resulting in larger uncertainties.

3.4.1 Iterative Weighting

The first strategy I have used is an *iterative weighting* technique. Since a 2-dimensional fine binning would result in too many bins with too low statistics, a 1-dimensional

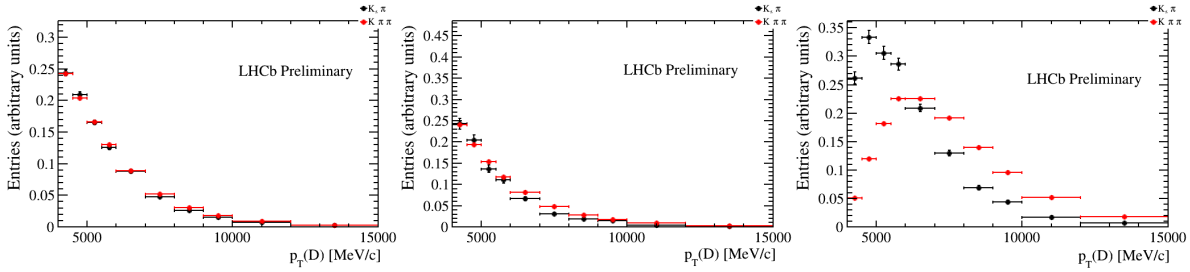

(a) $p_T(D)$ Full sample (b) $p_T(D)$ TIS sample (c) $p_T(D)$ TOS sample

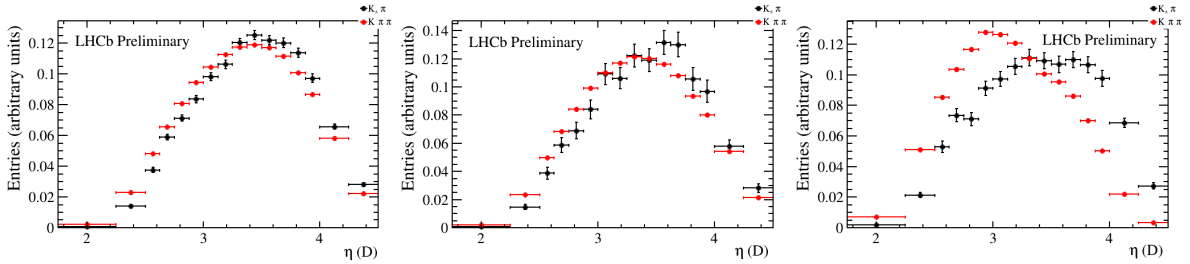

(d) $\eta(D)$ Full sample (e) $\eta(D)$ TIS sample (f) $\eta(D)$ TOS sample

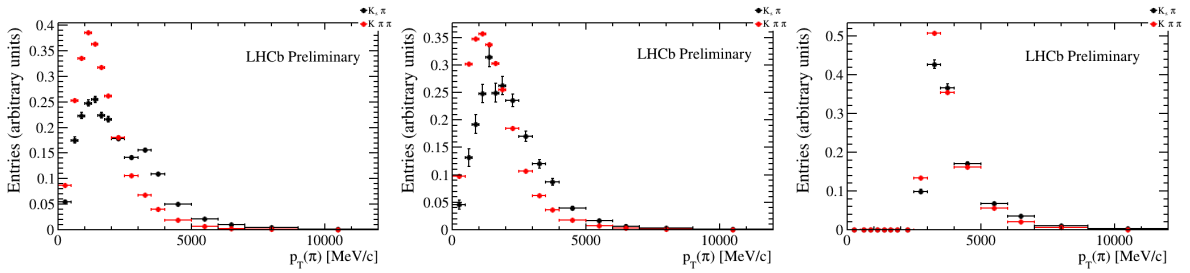

(g) $p_T(\pi)$ Full sample (h) $p_T(\pi)$ TIS sample (i) $p_T(\pi)$ TOS sample

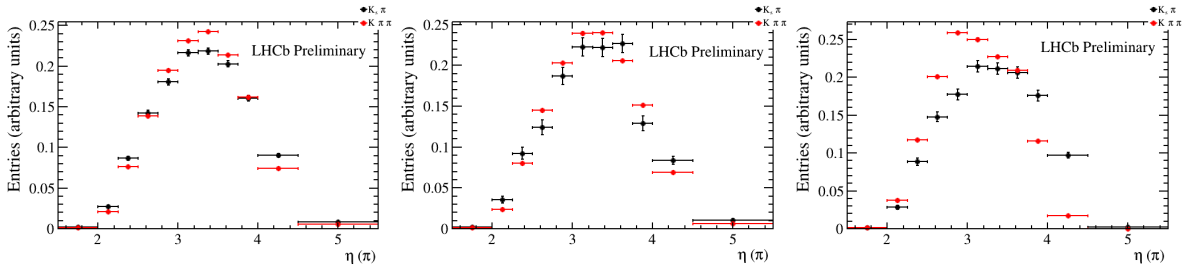

(j) $\eta(\pi)$ Full sample (k) $\eta(\pi)$ TIS sample (l) $\eta(\pi)$ TOS sample

Figure 3.8: Kinematic distributions normalized of D^+ and π^+ for the different sample in magnet up configuration. From left to right first row: distributions of transverse momentum $p_T(D^+)$ in the full sample, in the TIS sample and in the TOS sample; second row: distribution of pseudorapidity $\eta(D^+)$ in the full sample, in the TIS sample and in the TOS sample. The third and fourth row present the same distributions for π^+. In each plot in black the $D^+ \to K^-\pi^+\pi^+$ decay and in red the $D^+ \to K^0_s\pi^+$ decay.

weighting seemed to be more optimal to avoid empty bins. In this technique the weighting procedure is divided in steps. During each step, only one kinematic variable is weighted at a time. The weighting is done in the following order: $\eta(D^+)$, $p_T(D^+)$, $\eta(\pi^+)$ and lastly $p_T(\pi^+)$. After each step, the resulting weights are applied to the kinematic distributions before computing the weights of the successive step. The resulting weight will be a product of the weights of each step. This procedure can be iterated as long as each step improve the overall compatibility of distributions.

In each step weights are computed as

$$w^i = \frac{N_{\text{tot}}(K\pi\pi)N^i_{\text{bin}}(K_s\pi)}{N_{\text{tot}}(K_s\pi)N^i_{\text{bin}}(K\pi\pi)}, \tag{3.12}$$

with N_{tot} the total number of events in the sample and N_{bin} the number of events in the bin for which the weight is being computed. Each event in the bin is then assigned this w_i weight before proceeding to the next step. The resulting distributions for which both s-weights and kinematic weights are applied are presented in Fig. 3.9 for ten iteration of the weighting procedure. The TIS and TOS sample are weighted independently one of each other.

This procedure produce kinematic distributions with remarkable matching, as presented in Fig. 3.9, but also present some issues. While it performs effectively for these distributions it does not work as good when data are binned in K^- momentum, that is required to produce a differential measurement of the detection asymmetry. In fact, in that case the weighting step for π^+ produces weights that negatively affect the weights of the D^+ distribution, and vice verse, so that after each iteration the overall weighting is not improved. Furthermore, the TOS sample has less matching in η variables than TIS sample.

For this reason a more sophisticated version of this technique have been studied.

3.4.2 2-Dimensional Weighting

The second strategy adopted is a slight variation of the iterative weighting. To improve the weighting for both particles simultaneously a 2-dimensional weighting is applied. Again the weighting procedure is performed in several steps, i.e. a 2-dimensional reweighting on $\eta(D)$ and $\eta(\pi)$ which is followed by a 2-dimensional weighting on $p_T(D)$ and $p_T(\pi)$. The computation of the weights in each bin is performed with Eq. 3.12. The aforementioned procedure is repeated iteratively if the matching of kinematic distributions of kinematic distributions is not optimal.

In this approach, the 2-dimensional histograms have a coarser binning with respect to the 1-dimensional shown in Fig. 3.9. Also, the kinematics cut have been changed to either exclude bins with negative entries, due to negative s-weights, or to exclude low statistic regions, that could negatively affect weights quality but do not have much physical

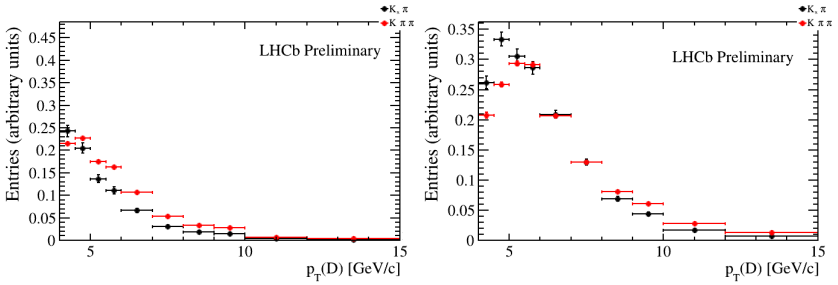

(a) $p_T(D)$ TIS sample

(b) $p_T(D)$ TOS sample

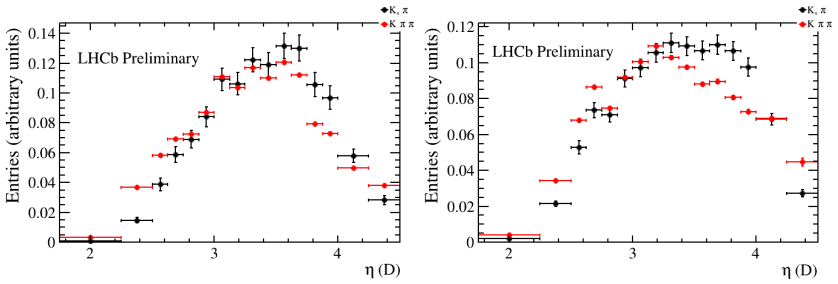

(c) $\eta(D)$ TIS sample

(d) $\eta(D)$ TOS sample

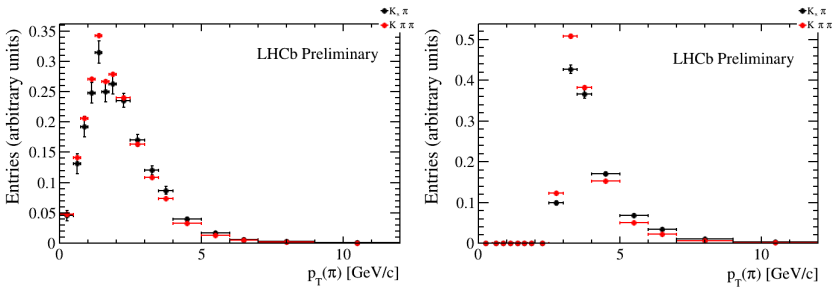

(e) $p_T(\pi)$ TIS sample

(f) $p_T(\pi)$ TOS sample

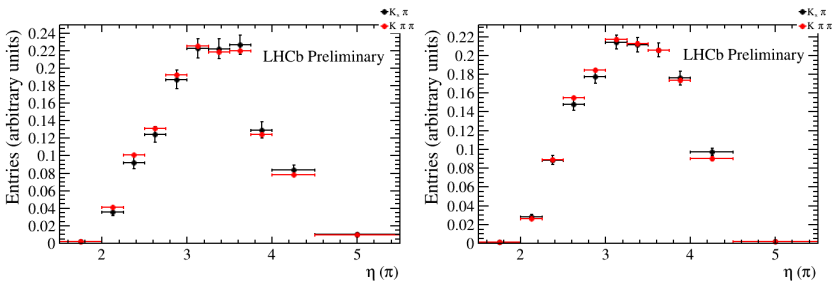

(g) $\eta(\pi)$ TIS sample

(h) $\eta(\pi)$ TOS sample

Figure 3.9: Kinematic distribution of D^+ and π^+ after 10 iteration of the iterative weights' technique.

Variable	TIS sample	TOS sample
$p_T(D^{\pm})$ [GeV]	$3 < p_T < 10$	$4 < p_T < 10$
$\eta(D^{\pm})$	$2.5 < \eta < 4.5$,	$2.5 < \eta < 4.5$
	if $\eta(\pi) < 2.5 \Rightarrow 2.5 < \eta(D) < 3$	
$p_T(\pi^{\pm})$ [GeV]	if $3 < p_T(D) < 4 \Rightarrow 0 < p_T(\pi) < 3$	$2.5 < p_T < 10$
	if $4 < p_T(D) < 5 \Rightarrow 0 < p_T(\pi) < 4$	
	if $p_T(D) > 5 \Rightarrow 0 < p_T(\pi) < 5$	
$\eta(\pi^{\pm})$	$2 < \eta < 5$	$2 < \eta < 5$

Table 3.4: Kinematics cuts applied to the two samples, for both polarity, for 2-dimensional weighting.

importance, i.e. very high momentum particle or turn-on regions in p_T distributions due to TOS selections.

The new kinematic cuts can be divided in two categories: applied to the whole TIS or TOS sample, or applied to an individual bin of charged kaon momentum. In this second case the cuts will be presented later on. The kinematic cuts applied to the whole samples are reported in Tab. 3.4. These cuts are applied to both decay modes.

The 2-dimensional distributions before and after the weighting are reported in Fig. 3.10 for TIS sample and magnet up.

This method produced kinematic distributions that are more compatible. Iterating the procedure however did not improve the weighting, so only one iteration has been applied. The most interesting resulting 1-dimensional histograms are reported in Fig. 3.11. Here can be seen that this method is working better in the TIS sample, i.e. in the η distributions that were the more problematic in the previous section. This method shows a non-perfect agreement between the kinematic distributions in the TOS sample.

An additional preliminary weighting is adopted as reported in the following Subsection.

Finally, the $K\pi\pi$ sample is divided in bins of charged kaon momentum. For each bin of both TIS and TOS, an independent reweighting is performed on the corresponding $K_s\pi$ sample. As stated before in each bin of kaon momentum different kinematic cuts are applied. These additional cuts are reported in Tab. 3.5. For each bin the same process for the whole sample is repeated.

3.4.3 Additional Reweighting

Since for some bins in the TOS sample applying only the 2-dimensional weighting is not enough to obtain distributions in good agreement an additional weighting step is performed before the 2-dimensional weighting. In this step, instead of weighting $K\pi\pi$ sample on the K_s^0 sample, the opposite is done. To avoid losing too much statistic of $K_s\pi$ in this step an even coarser binning is applied. This allows to start the 2-dimensional

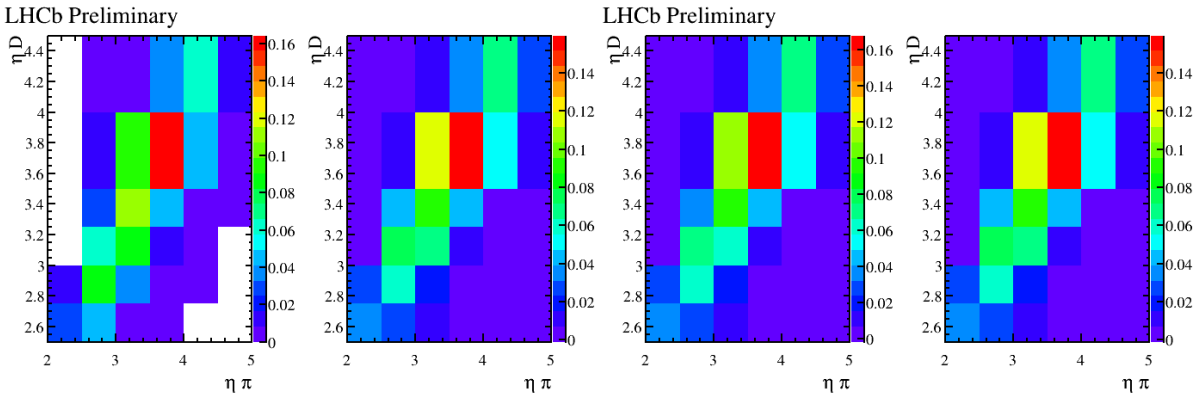

(a) $\eta(D)$ and $\eta(\pi)$ before weighting

(b) $\eta(D)$ and $\eta(\pi)$ after weighting

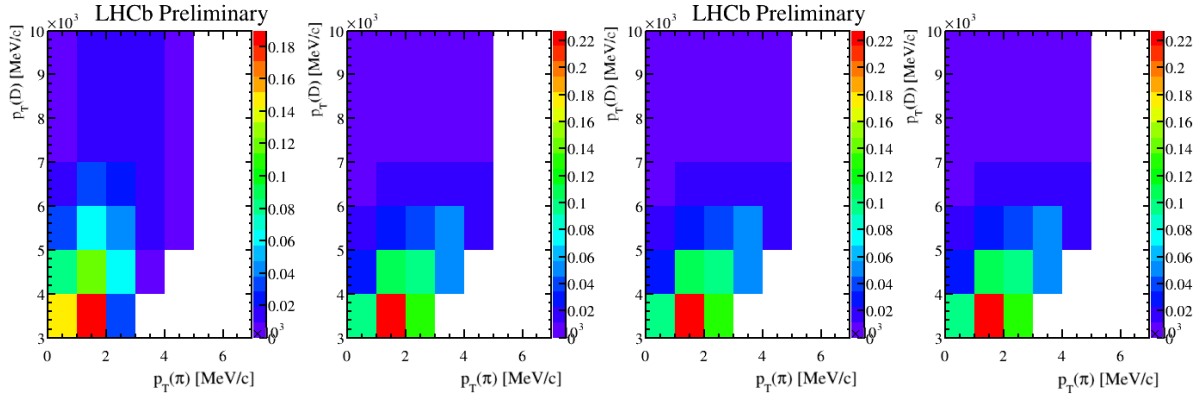

(c) $p_T(D)$ and $p_T(\pi)$ before weighting

(d) $p_T(D)$ and $p_T(\pi)$ after weighitng

Figure 3.10: 2-Dimensional distributions of $\eta(D)$ and $\eta(\pi)$ and $p_T(D)$ and $p_T(\pi)$ for TIS sample and magnet up. On the left of each plot the $K\pi\pi$ decay mode is shown and on the right the $K_s\pi$ one.

$p(K^{\pm})$ bin	TIS	TOS
$10-15$ GeV	No additional cuts	No additional cuts
$15-20$ GeV	No additional cuts	No additional cuts
$20-25$ GeV	No additional cuts	Excluded events in $8 < p_T(D) < 9$ GeV and $7 < p_T(\pi) < 8$ GeV
$25-30$ GeV	If $\eta(\pi) < 3 \Rightarrow \eta(D) < 4$	No additional cuts
$30-40$ GeV	If $\eta(\pi) < 3 \Rightarrow \eta(D) < 4$	No additional cuts
$40-60$ GeV	If $\eta(\pi) < 3 \Rightarrow \eta(D) < 4$ If $\eta(\pi) > 4.5 \Rightarrow \eta(D) > 3.5$	If $\eta(\pi) < 3 \Rightarrow \eta(D) < 3.25$

Table 3.5: Additional cut applied to the bins of $p(K^{\pm})$ for each sample. These cuts are also applied to the $K_s\pi$ mode independently in each bin before the reweighting step.

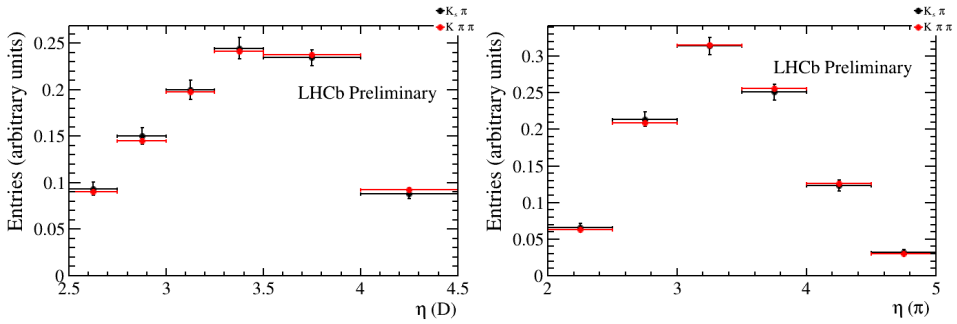

(a) $\eta(D)$ TIS sample

(b) $\eta(\pi)$ TIS sample

(c) $\eta(D)$ TOS sample

(d) $p_T(D)$ TOS sample

Figure 3.11: Some distributions for both TIS and TOS sample with 2-dimensional reweighting for magnet up sample. In black $K_s\pi$ decay mode, in red $K\pi\pi$ one.

Sample	TIS Sample [%]	TOS Sample [%]
Magnet Up	$A^{\rm det} = -1.8 \pm 3$	$A^{\rm det} = 11 \pm 5$
Magnet Down	$A^{\rm det} = -2 \pm 2$	$A^{\rm det} = -15 \pm 3$
Magnet Average	$A^{\rm det} = -1.9 \pm 1.9$	$A^{\rm det} = -2.1 \pm 2.8$

Table 3.6: Detection asymmetries $A^{\rm det}$ for the full sample of TIS and TOS, in different magnet polarieties.

weighting procedure from more similar distributions, thus simplifying the procedure. The weights are calculated using

$$w^i = \frac{N_{\rm tot}(K_s\pi) N^i_{\rm bin}(K\pi\pi)}{N_{\rm tot}(K\pi\pi) N^i_{\rm bin}(K_s\pi)}. \tag{3.13}$$

Only not-well-weighted bins have been processed, namely the bin corresponding to 10 GeV $< p(K^-) <$ 15 GeV kaon momentum for magnet up polarity. The resulting distributions are reported in Fig. 3.12.

3.5 Fit to Model and Determination of $A^{\rm det}(K\pi)$

After the reweighting step a maximum likelihood is performed to determine the raw asymmetries $A^{\rm raw}(K\pi\pi)$ and $A^{\rm raw}(K_s\pi)$, independently on each bin and on the whole samples.

The function used in these fits is:

$$\begin{aligned} N_{bckg}(a_0 + a_1 x) + \frac{1}{2} N_{sig}[&(1 + A_{raw})(f^+_{sig} G^+_1(\mu^+, \sigma^+_1) + (1 - f^+_{sig}) G^+_2(\mu^+, \sigma_2)) \\ &+(1 - A_{raw})(f^-_{sig} G^-_1(\mu^-, \sigma^-_1) + (1 - f^-_{sig}) G^-_2(\mu^-, \sigma_2))]. \end{aligned} \tag{3.14}$$

To eliminate possible additional effects due to misalignment or acceptance that are dependent on the magnet polarity a magnet average detection asymmetry is computed as:

$$A^{\rm det}_{\rm avg} = \frac{A^{\rm det}_{\rm up} + A^{\rm det}_{\rm down}}{2}. \tag{3.15}$$

The resulting asymmetries for the full samples are reported in Tab. 3.6. The invariant mass distributions and their fits for the determination of these quantities are reported in Fig. 3.13-3.14. A differential measurement of the detection asymmetry has been performed in bins of $p(K^\pm)$ for both samples, and it is reported in Fig. 3.15.

A χ^2 test for the hypothesis of constant detection asymmetry is performed and the value of the asymmetry for which χ^2 is minimum has been reported in Fig. 3.15.

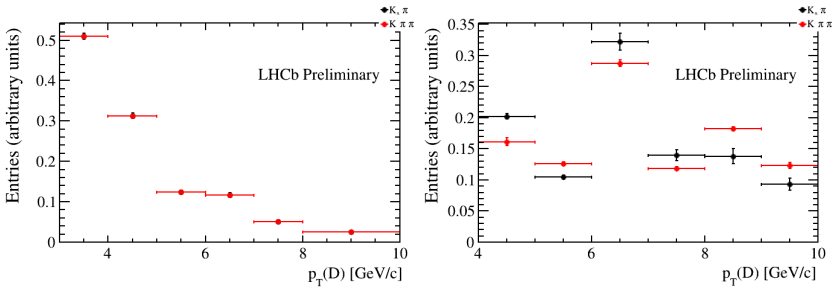

(a) $p_T(D)$ TIS sample

(b) $p_T(D)$ TOS sample

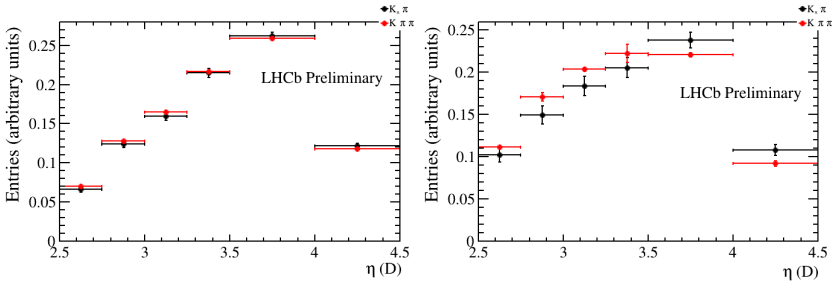

(c) $\eta(D)$ TIS sample

(d) $\eta(D)$ TOS sample

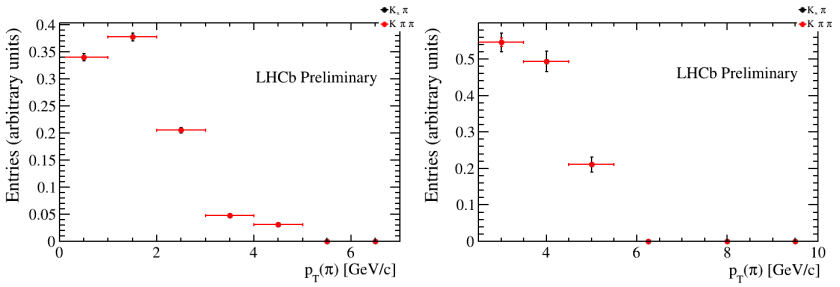

(e) $p_T(\pi)$ TIS sample

(f) $p_T(\pi)$ TOS sample

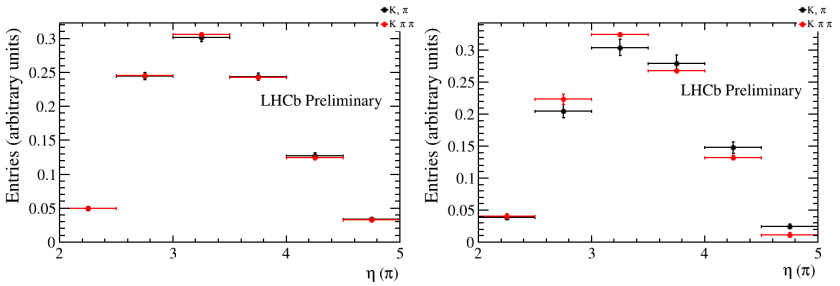

(g) $\eta(\pi)$ TIS sample

(h) $\eta(\pi)$ TOS sample

Figure 3.12: Kinematic distributions for the bin in kaon momentum 10 GeV $< p(K^-) <$ 15 GeV for magnet up polarity with additional preliminary weighting. In black $K_s\pi$ decay mode and in red $K\pi\pi$.

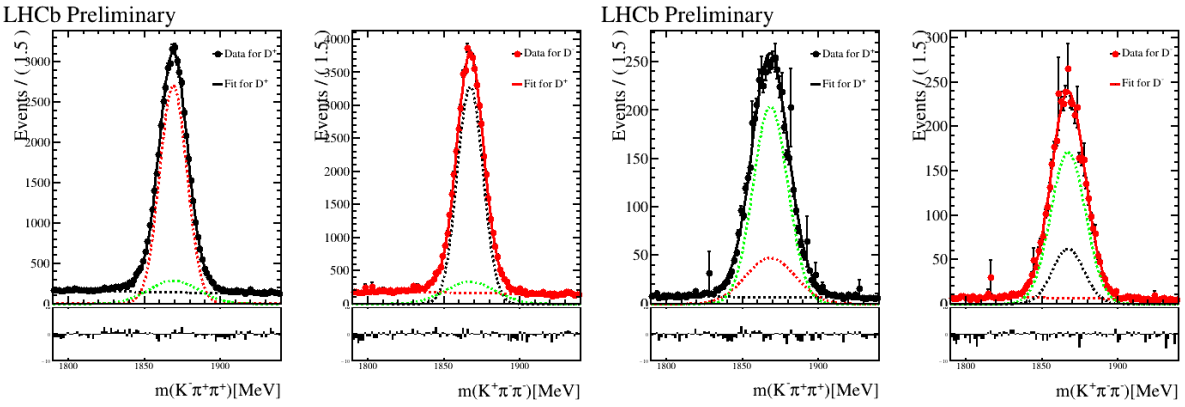

(a) TIS Magnet up $K\pi\pi$

(b) TOS Magnet up $K\pi\pi$

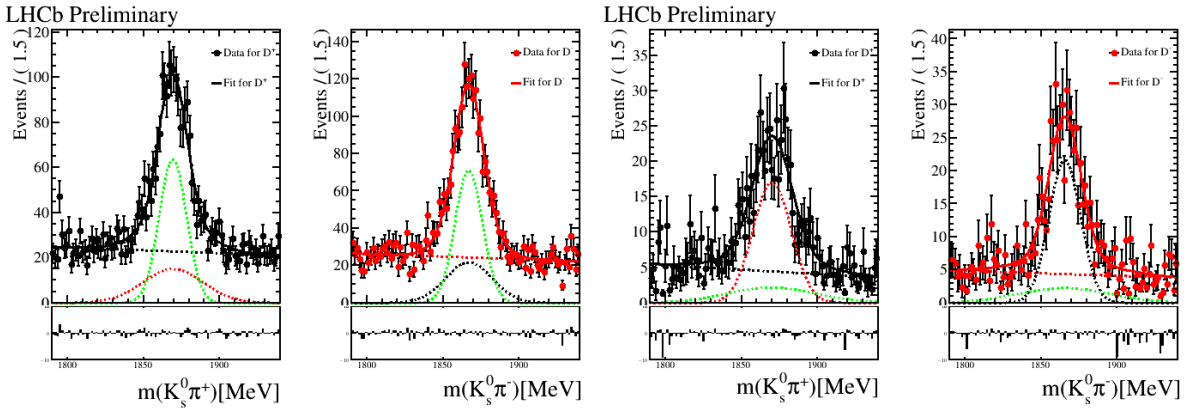

(c) TIS Magnet up $K_s\pi$

(d) TOS Magnet up $K_s\pi$

Figure 3.13: Invariant mass distribution with fits for the determination of detection asymmetries for full samples for magnet up polarity. Some events have been assigned a high weight as it can be observed in TOS sample for $K\pi\pi$.

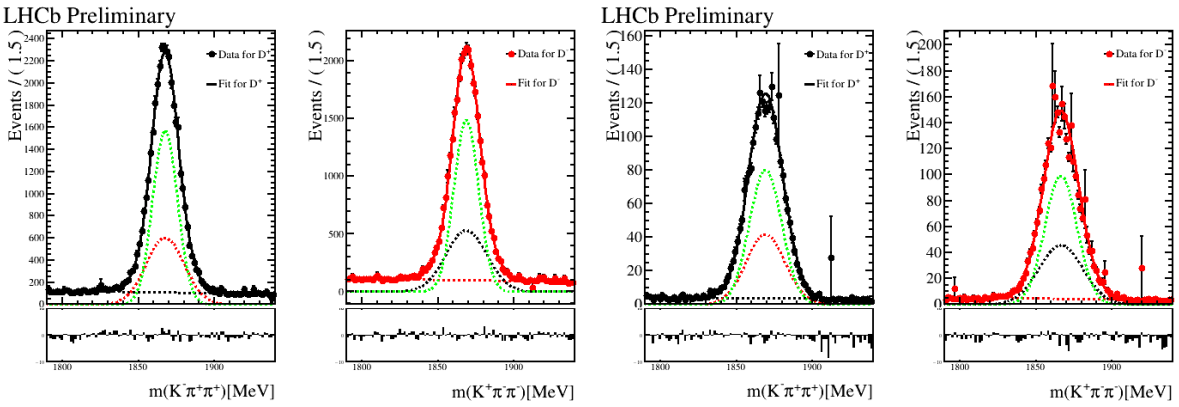

(a) TIS Magnet down $K\pi\pi$

(b) TOS Magnet down $K\pi\pi$

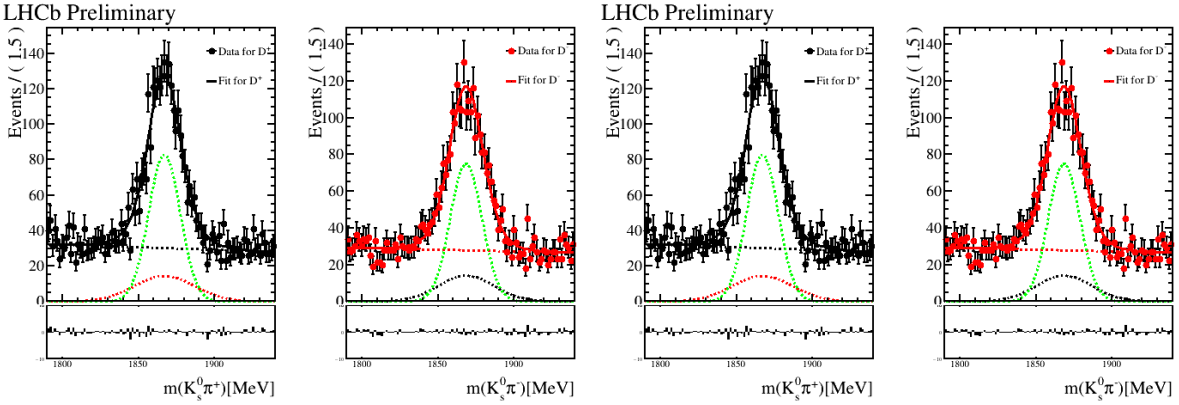

(c) TIS Magnet down $K_s\pi$

(d) TOS Magnet down $K_s\pi$

Figure 3.14: Invariant mass distribution with fits for the determination of detection asymmetries for full samples for magnet down polarity.

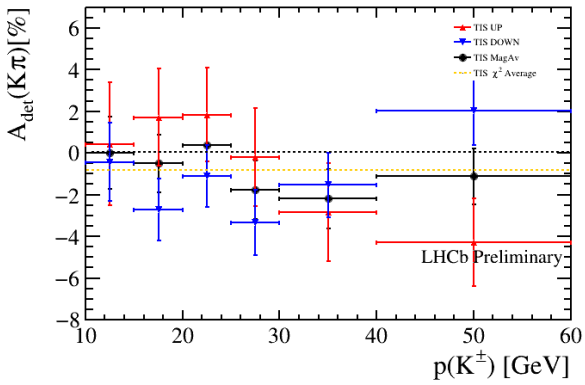

(a) TIS sample

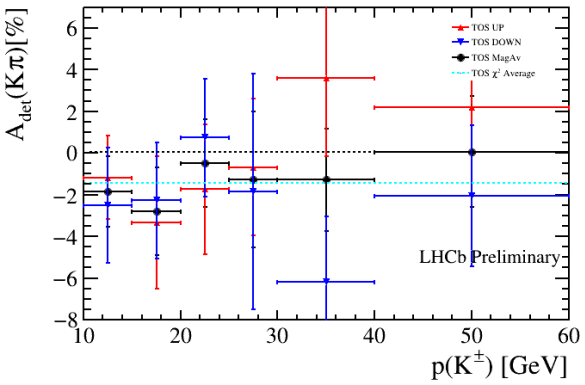

(b) TOS sample

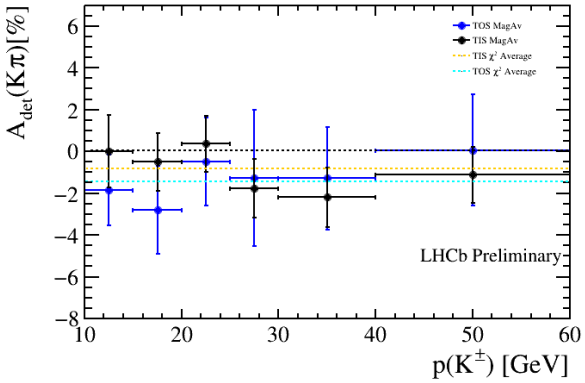

(c) Comparison of both samples

Figure 3.15: Differential measurement of A^{det} for both samples and compared. For the two top plots in red magnet up measurements, in blue magnet down measurements and in black the magnet average. For TIS sample in orange the value for which the χ^2 is minimum, for the TOS sample in cyan. In the last plot the comparison between TIS, in black, and TOS, in blue, along with minimum χ^2 value.

3.6 Uncertainty Estimation and Method Validation

To properly account for the weighting events in the uncertainty estimation and to perform controls on the fit itself, additional studies are performed. In particular, to check if the fit is either biased or wrongly estimates the uncertainty *Monte Carlo (MC) toys* are studied. After the fit of the previous section, the resulting parameters are saved and used to generate 10000 additional datasets of equal size as the one fitted. Then weights are shuffled and randomly assigned to the events. To each new dataset is performed a new fit and a new raw asymmetry $A_{\rm fit}^{\rm raw}$ and uncertainty $\sigma_{\rm fit}$ are extracted, from which we compute the pull of the dataset

$$\text{pull} = \frac{A_{\rm fit}^{\rm raw} - A_{\rm gen}^{\rm raw}}{\sigma_{\rm fit}}, \tag{3.16}$$

in which $A_{\rm gen}^{\rm raw}$ is the raw asymmetry for the generation step, i.e. the one from the first fit, and $\sigma_{\rm fit}$ is the uncertainty obtained from the fit to the generated dataset.

If the fit is correct we expect the pulls to be a normal Gaussian. To check this the resulting pull distribution is fitted to a Gaussian. If $\sigma_{\rm gaus}$ is different from 1 we can understand if the uncertainty has been overestimated or underestimated. On the other hand if $\mu_{\rm gaus}$ is different from 0 we can understand if the fit is biased or unbiased.

In Fig. 3.16 is reported the distribution of pulls for the TIS sample, $K\pi\pi$ decay mode and magnet up polarity. After a fit to a Gaussian the resulting parameters are:

- $\mu_{\rm gaus} = 0.074 \pm 0.009$ close to 0 but not exactly 0 so the fit introduce a small bias.
- $\sigma_{\rm gaus} = 0.851 \pm 0.006$ lesser than 1 meaning that the uncertainty on the asymmetry is overestimated.

3.7 Results

During these thesis studies, the measurement of detection asymmetry $A^{\rm det}$ has been measured for both trigger channels. For the full samples the resulting asymmetries are:

$$\begin{aligned} A_{\rm TIS}^{\rm det} &= (-1.9 \pm 1.9)\%, \\ A_{\rm TOS}^{\rm det} &= (-2.1 \pm 2.8)\%. \end{aligned}$$

In these results the asymmetry of neutral kaon has not been accounted for as well as small bias and uncertainties overestimation as shown in Sec. 3.6.

From the differential measurements in bins of $p(K^{\pm})$ the minimum χ^2 reduced value are reported in Tab. 3.7

In the differential case, the p-value for the null hypothesis of $A^{\rm det} = 0$ is $p\text{-}value \simeq 1$ for TIS and $p\text{-}value = 0.8497$ for TOS, so both measurement are compatible with the null hypothesis.

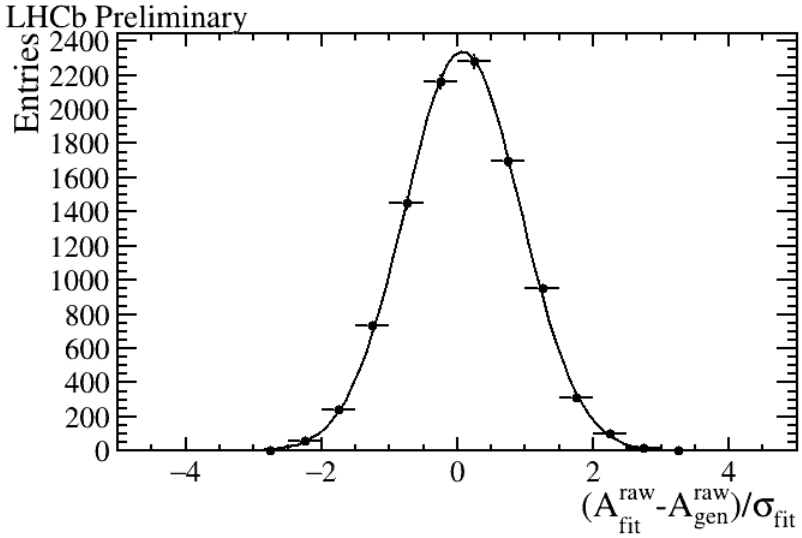

Figure 3.16: Distribution of pulls for TIS sample, $K\pi\pi$ decay mode and magnet up polarity, fitted to a Gaussian.

	TIS sample	TOS sample
Minimizing value:	$A^{\text{det}} = -0.819\%$	$A^{\text{det}} = -1.439\%$
Reduced χ^2 at minimum:	$\chi^2/n_{dof} = 0.000122$	$\chi^2/n_{dof} = 0.221$

Table 3.7: Minimum value of χ^2 for both sample of the differential measurements.

3.7.1 Outlooks and Future Applications

Even if these measurements are not yet competitive, with additional statistics provided by Run 3 data taking campaign they will become useful to measure production asymmetries. In fact, during these studies only the data taken in 2022 were analysed. In the future the whole Run 3 data taking campaign will be analysed.

After the refinement of this analysis these studies can be used to measure production asymmetry as described in Eq. 3.1. These same techniques presented in this thesis can also be easily translated to production asymmetry measurements due to the similar experimental signature of these asymmetries. Once also this measurement of production asymmetry will be performed it will be a very useful input parameter in future CP violation studies as well as in other studies, such as QCD models validation.

Conclusions

The main goal of the thesis work is to measure detection asymmetry for $K^-\pi^+$ mesons. This measurement is a fundamental input parameter for production and CP violation asymmetries measurements. CP asymmetries are powerful probes for physics beyond the Standard Model, while production asymmetries are input parameters in validation of non-perturbative QCD models and detector validation.

Along with this, other preliminary studies useful for understanding misalignment effects have been performed.

The main measurement of detection asymmetry have been performed with Run 3 data collected by LHCb during 2022 data taking campaign. The $D^+ \to K^-\pi^+\pi^+$ and $D^+ \to K^0_s\pi^+$ decays have been analysed to extract the detection asymmetry. The data sample have been divided in two samples depending on the trigger configuration, i.e. when the decays are triggered on the signal track (TOS) or independently from the signal (TIS). Each of these two samples have been additionally split depending on the magnet polarity. The detection asymmetry has been measured independently in each of the two samples along with a differential measurement in bins of momentum of the kaon.

The resulting asymmetries are

$$\begin{aligned} A^{\text{det}}_{\text{TIS}} &= (-1.9 \pm 1.9)\%, \\ A^{\text{det}}_{\text{TOS}} &= (-2.1 \pm 2.8)\%. \end{aligned}$$

both compatible with zero. Including additional statistics from the full Run 3, the measurement will become more precise for future CP violation measurements.

Bibliography

[1] I. I. Bigi and A. I. Sanda. *CP Violation*. 2nd ed. Cambridge University Press, 2009. DOI: 10.1017/CBO9780511581014.

[2] M. D. Schwartz. *Quantum Field Theory and the Standard Model*. Cambridge University Press, 2013. DOI: 10.1017/9781139540940.

[3] C. Quigg. *Gauge Theories of the Strong, Weak, and Electromagnetic Interactions: Second Edition*. 2nd ed. Princeton University Press, 2013. ISBN: 0691135487. URL: http://www.jstor.org/stable/j.ctt3fgx94 (visited on 10/02/2023).

[4] M. E. Peskin and D. V. Schroeder. *An Introduction to quantum field theory*. Reading, USA: Addison-Wesley, 1995. ISBN: 978-0-201-50397-5.

[5] Particle Data Group, R. L. Workman et al. "Review of Particle Physics". In: *PTEP* 2022 (2022), p. 083C01. DOI: 10.1093/ptep/ptac097.

[6] The LHCb Collaboration, R. Aaij et al. "Observation of CP Violation in Charm Decays". In: *Phys. Rev. Lett.* 122.21 (2019), p. 211803. DOI: 10.1103/PhysRevLett.122.211803. arXiv: 1903.08726 [hep-ex].

[7] Y. Amhis et al. "Averages of b-hadron, c-hadron, and τ-lepton properties as of 2021". In: *Phys. Rev. D* 107 (2023), p. 052008. DOI: 10.1103/PhysRevD.107.052008. arXiv: 2206.07501 [hep-ex].

[8] E. Braaten, Y. Jia, and T. Mehen. "Leading-Particle Effect from Heavy-Quark Recombination". In: *Physical Review Letters* 89.12 (Aug. 2002). DOI: 10.1103/physrevlett.89.122002. URL: https://doi.org/10.1103%2Fphysrevlett.89.122002.

[9] R. Vogt and S. Brodsky. "Charmed hadron asymmetries in the intrinsic charm coalescence model". In: *Nuclear Physics B* 478.1 (1996), pp. 311–332. ISSN: 0550-3213. DOI: https://doi.org/10.1016/0550-3213(96)00380-X. URL: https://www.sciencedirect.com/science/article/pii/055032139600380X.

[10] The LHCb Collaboration, R. Aaij et al. "Measurement of the $D^{\pm}$ production asymmetry in 7 TeV pp collisions". In: *Phys. Lett. B* 718 (2013), pp. 902–909. DOI: 10.1016/j.physletb.2012.11.038. arXiv: 1210.4112 [hep-ex].

[11] The LHCb Collaboration, R. Aaij et al. "Measurement of $D_s^{\pm}$ production asymmetry in pp collisions at $\sqrt{s} = 7$ and 8 TeV". In: *JHEP* 08 (2018), p. 008. DOI: 10.1007/JHEP08(2018)008. arXiv: 1805.09869 [hep-ex].

[12] The LHCb Collaboration, R. Aaij et al. *The LHCb Upgrade I*. 2023. arXiv: 2305.10515 [hep-ex].

[13] The LHCb Collaboration, A. A. A. Jr et al. "The LHCb Detector at the LHC". In: *Journal of Instrumentation* 3.08 (Aug. 2008), S08005. DOI: 10.1088/1748-0221/3/08/S08005. URL: https://dx.doi.org/10.1088/1748-0221/3/08/S08005.

[14] "LHCb detector performance". In: *International Journal of Modern Physics A* 30.07 (Mar. 2015), p. 1530022. DOI: 10.1142/s0217751x15300227. URL: https://doi.org/10.1142%2Fs0217751x15300227.

[15] L. Evans and P. Bryant. "LHC Machine". In: *Journal of Instrumentation* 3.08 (Aug. 2008), S08001. DOI: 10.1088/1748-0221/3/08/S08001. URL: https://dx.doi.org/10.1088/1748-0221/3/08/S08001.

[16] J. Haffner. "The CERN accelerator complex. Complexe des accélérateurs du CERN". In: (2013). General Photo. URL: https://cds.cern.ch/record/1621894.

[17] The LHCb Collaboration, S. Amato et al. *LHCb magnet: Technical Design Report*. Technical design report. LHCb. Geneva: CERN, 2000. URL: https://cds.cern.ch/record/424338.

[18] The LHCb Collaboration, *LHCb VELO Upgrade Technical Design Report*. Tech. rep. 2013. URL: https://cds.cern.ch/record/1624070.

[19] The LHCb Collaboration, *LHCb Tracker Upgrade Technical Design Report*. Tech. rep. 2014. URL: https://cds.cern.ch/record/1647400.

[20] The LHCb Collaboration, *LHCb PID Upgrade Technical Design Report*. Tech. rep. 2013. URL: https://cds.cern.ch/record/1624074.

[21] The LHCb Collaboration, *LHCb Trigger and Online Upgrade Technical Design Report*. Tech. rep. 2014. URL: https://cds.cern.ch/record/1701361.

[22] "RTA and DPA dataflow diagrams for Run 1, Run 2, and the upgraded LHCb detector ". In: (2020). URL: https://cds.cern.ch/record/2730181.

[23] A. Davis et al. *Measurement of the instrumental asymmetry for $K^-\pi^+$-pairs at LHCb in Run 2*. Tech. rep. Geneva: CERN, 2018. URL: http://cds.cern.ch/record/2310213.

[24] "Measurement of the time-integrated CP asymmetry in $D^0 \to K^-K^+$ decays". In: (Sept. 2022). arXiv: 2209.03179 [hep-ex].

[25] *ROOT Data Analysis Framework*. https://root.cern.

[26] M. Pivk and F. L. Diberder. ": A statistical tool to unfold data distributions". In: *Nuclear Instruments and Methods in Physics Research Section A: Accelerators, Spectrometers, Detectors and Associated Equipment* 555.1-2 (Dec. 2005), pp. 356–369. DOI: 10.1016/j.nima.2005.08.106. URL: https://doi.org/10.1016%2Fj.nima.2005.08.106.